1-1-2021

Stratigraphy and Geochemistry of Paleocene-Aged Bauxites from North Mississippi

Timothy Brendan Clark
University of Mississippi

STRATIGRAPHY AND GEOCHEMISTRY OF PALEOCENE-AGED BAUXITES FROM NORTH MISSISSIPPI

A Thesis

presented in partial fulfillment of requirements

for the degree of Master of Science

in the Department of Geology and Geological Engineering at The University of Mississippi

by

TIMOTHY B. CLARK

August 2021

ABSTRACT

Bauxite is a heavily-mined aluminum ore that forms through the relative depletion of silica to aluminum. In North Mississippi, bauxite occurring within the Upper Midway and Lower Wilcox groups has been the subject of study for over a century. Despite the abundance and duration of research, controversy surrounds the subjects of bauxite genesis and economic value. The last detailed study of North Mississippi bauxite was in the 1980's, so the goal of this project is to apply newly available technologies and modern hypotheses on bauxite formation to refine and obtain new data. Fieldwork observations yielded pisoliths, horizonation, and possible rhizoliths, which support a lateritic genesis at the most well exposed outcrop, which is located in Pontotoc County and mapped as the Upper Midway Group. Additionally, stratigraphic trends in percentages of SiO_2, Al_2O_3, and Fe_2O_3 at this location closely resembled that of a typical lateritic bauxite profile reflecting the depletion of SiO_2 and enrichment of Fe_2O_3 upsection. Abundances of chromium (Cr) and nickel (Ni) as well as percentages of zirconium (Zr), gallium (Ga), and chromium (nickel) (Cr(Ni)) determined the bauxite protolith was acidic and/or sedimentary and that bauxites were of the high-iron lateritic variety. This aligned with the occurrence of siderite (iron carbonate) in the interpreted protolith as well as ratios of lanthanum to yttrium that indicated an acidic paleoenvironment throughout the section. Lastly, stable isotope data confirmed prior hypotheses of a warm paleoclimate and indicated subaerial exposure of the interpreted parent material. A comparison with the reworked bauxite of the Lower Wilcox Group found that pisoliths were different in regards to structure and chemistry, supporting the hypothesis that these originated in a separate event or under different conditions.

LIST OF ABBREVIATIONS AND SYMBOLS

Fm	Formation
Mbr	Member
ME	Mississippi Embayment
GOM	Gulf of Mexico
SEM	Scanning electron microscope
EDS	Energy dispersive spectroscopy
UM	University of Mississippi
LOI	Loss on ignition
LOI_{105}	LOI after 105°C ignition
LOI_{550}	LOI after 550°C ignition
LOI_{950}	LOI after 950°C ignition
LOI_{total}	Total LOI
XRD	X-ray diffraction
CD	citrate-dithionite
ICP-OES	inductively coupled plasma – optical emission spectrometry
ICP-MS	inductively coupled plasma – mass spectrometry
IR-MS	isotope ratio mass spectrometer
SMU	Southern Methodist University
SMOW	standard mean ocean water

VPDB	Vienna Peedee Belemnite
OC	organic carbon
IC	inorganic carbon
HREE	Heavy Rare Earth Element
LREE	Light Rare Earth Element
Mt	Metric tons
Ma	Mega annum
kV	Kilovolts
mA	Milliamperes
RPM	Revolutions per minute
V	Vogt's Residual Index
STI	Silica-Titania Index
CIA	Chemical Index of Alteration
CIW	Chemical Index of Weathering
PIA	Plagioclase Index of Alteration
WIP	Weathering Index of Parker
S/H	Supergene/Hypogene

ACKNOWLEDGEMENTS

I would like to acknowledge my advisor Dr. Brian F. Platt as well as my committee members Dr. Inoka Widanagamage and Dr. Jennifer Gifford. I would also like to thank the University of Mississippi Department of Geology and Geological Engineering for employing me as a teaching assistant, without which I would not have been able to finance my education. For his assistance during the completion of field work, I would like to express my gratitude to my fellow graduate student Trevor Dempsey. I would like to acknowledge Dr. John Robbins and Dr. Ian Richards at Southern Methodist University for their assistance during analysis of isotope composition as well as Dr. Vijayasankar Raman and Dr. Jason Hoeksema at the University of Mississippi for their help and expertise when analyzing samples using scanning electron microscopy. I would like to thank Cole Boren, for measuring the Arrow Road section, and to Dr. Charles Swann for showing my advisor the Arrow Road location years ago. This research would not be possible without funding provided by the Geological Society of America and the Society for Sedimentary Geology. I would like to acknowledge my older sister Joanna, also a Geologist, for serving as an excellent role model. Lastly, I would like to acknowledge my parents, Donald and Tracy, as well as Anna Conner for supporting me throughout the completion of this research.

TABLE OF CONTENTS

LIST OF TABLES

LIST OF FIGURES

1. INTRODUCTION

Bauxite is a sedimentary rock that has been enriched in Al-hydroxides, kaolinite, Fe-oxyhydroxide, and titanium-oxide due to the chemical weathering of an aluminosilicate parent rock (Mondillo et al., 2020). Berthier (1821) was the first to recognize bauxite and defined it as a rock with high Al content in the vicinity of Les Baux, France. Bauxite textures range from massive or earthy, nodular, pisolithic, oolitic, brecciated, botryoidal, cellular, platy, to vermicular (Patterson, 1967). The mineralogy of most bauxites is dominated by gibbsite, boehmite, and diaspore with subordinate amounts of goethite, hematite, kaolinite, and quartz (Hao et al., 2010; Mondillo et al., 2020). Galena, covellite, zircon, pyrite, calcium plagioclase, orthoclase, and albite may be present, but are less common (Hao et al., 2010; Mondillo et al., 2020). Such mineralogy will produce a weight percent (wt. %) of Al_2O_3, Fe_2O_3, and TiO_2 greater than 50% (Mondillo et al., 2020). The term 'bauxite' can be used in an economic context to describe an array of valuable materials based on their mineralogic and production of Al, Al_2O_3, and high-refractory materials (e.g., mullite, spinel; Valeton, 1972; Thompson, 1981). Elemental and mineralogical compositions of bauxites depend on parent rock chemistry and superimposed processes, respectively (Bogatyrev et al., 2009). The process by which bauxite forms (bauxitization) is accompanied by one or more of the following processes, each of which will yield different major oxide compositions: destruction of kaolinite, preservation of kaolinite, deferruginiztion, and dehydration (Beauvais, 1991).

There is abundant research dating back to the 1800s pertaining to the bauxites of north MS, yet there is still controversy regarding their stratigraphic position, genesis, and economic

value. Detailed research has not been conducted since 1981 (Thompson, 1981), so in this work, newly available technologies and updated theories on bauxite formation will be applied to reinterpret deposits in north MS.

Bauxite deposits are typically divided into three major genetic groups: sedimentary, lateritic, and karst. Shared properties of each group include the accumulation of Al caused by the separation of Al and Si, as well as chemical weathering being the of cause removal of silica, alkali earth metals, and Rare Earth Elements (REEs) from the parent rock or sediment (Bogatyrev et al., 2009). An alternative classification based on host rock geology and inferred genetic model for deposit formation divides bauxite into two groups: lateritic and karst (Mondillo et al., 2020).

Lateritic bauxites form as a result of *in situ* lateritic weathering typically occurring in tropical climates (Mondillo et al., 2020). Lateritization (the process by which rock is converted to lateritic soil) enriches the eluvial horizon of the lateritic profile in Al_2O_3, Fe_2O_3, and TiO_2 through leaching of soluble minerals (Freyssinet et al., 2005). Illuviation results in the accumulation of these leached minerals/ions in the lower portion of the profile (Freyssinet et al., 2005). Lateritic bauxites are divided into three categories based on pedogenic processes of occurrence, near the top of the profile: orthobauxites, metabauxites, and cryptobauxites (Table 1; Mondillo et al., 2020). Textural, lithological, and mineralogical variability are indicative of different degrees of leaching and hydration of unstable and soluble mineral phases (Freyssinet et al., 2005). This characterizes several pseudo-horizons within the classic lateritic bauxite profile (Fig. 2; Herrington et al., 2016). The lateritic profile exhibits three distinct layers: (1) bedrock, (2) basal clay-rich layer, and (3) upper lateritic residuum (Freeman and Donaldson, 2004).

Bedrock is the lowermost unit and represents the unweathered parent rock (Freeman and Donaldson, 2004). The clay-rich layer is divided into three zones: (1) saprolith, which is further

Table 1. The different types of lateritic and karst bauxites and their defining characteristics (Mondillo et al 2020).

	Type	Characteristics
Lateritic	Orthobauxites	Demonstrate classic lateritic bauxite profile; most widespread type
	Metabauxites	Al-rich and Fe-poor; quartz-poor protolith
	Cryptobauxites	Profile hidden below thick clay-rich cover
Karst	Mediterranean	Composition is almost completely bauxite
	Timan	Exhibits sub-planar morphology and contains bauxite, clay, and detritus
	Kazakhstan	Complex lithology; commonly fills deep karst structures
	Ariége	Two distinct pseudo-horizons: lower clayey-marly and upper bauxite
	Salento	Eroded and re-deposited bauxite and clays within karst structures
	Tulsk	No elevated Ti concentration

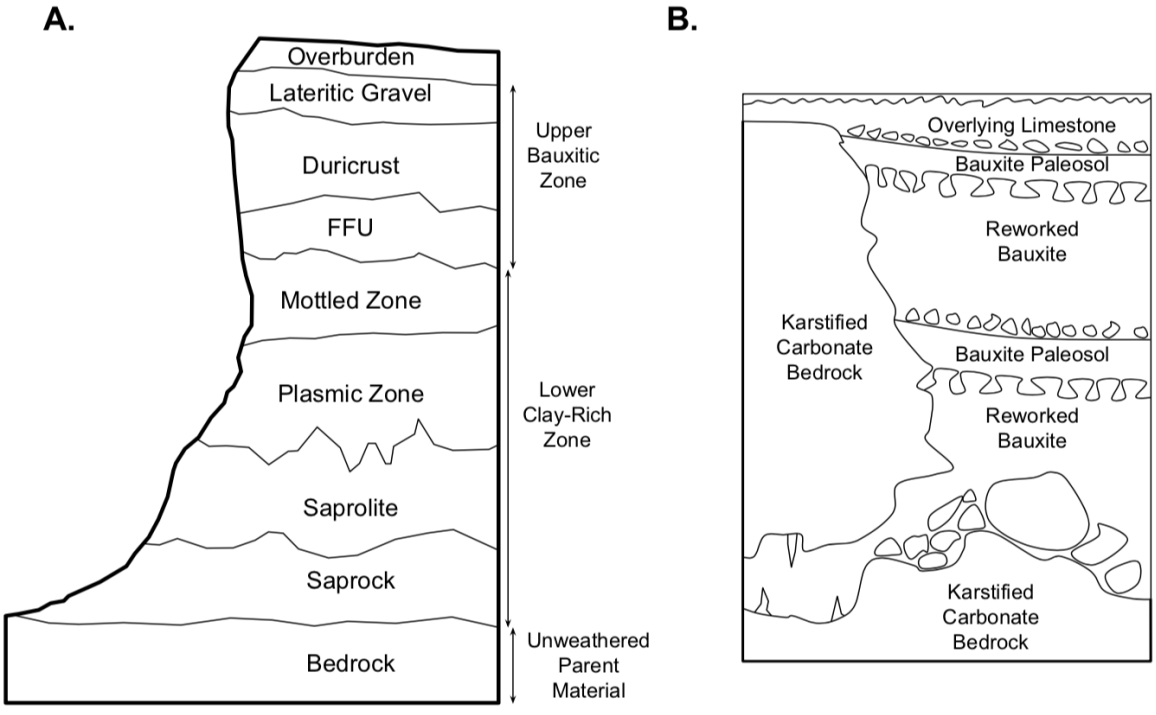

Figure 1. A: Pseudo-horizons present in the typical lateritic bauxite profile. B: Profile of the typical karst bauxite profile. Modified from Mondillo et al. (2020).

divided into the saprock and saprolite, (2) plasmic zone, and (3) mottled zone (Freeman and Donaldson, 2004; Mondillo et al., 2020). A lower Friable Fragmental Unit (FFU), middle duricrust, and upper lateritic gravel divides the upper lateritic residuum into three distinct layers (Freeman and Donaldson, 2004; Mondillo et al., 2020). Granular and nodular gibbsitic zones compose the lower and upper FFU, respectively (Freeman and Donaldson, 2004; Mondillo et al., 2020).

Karst bauxites are the second major group and differ from lateritic bauxites. Typically, they do not exhibit a classic lateritic profile, overlie karstified bedrock, and are allochthonous in origin (Fig. 1; Herrington et al., 2016; Mondillo et al., 2020). They usually form through one of three processes: (1) mechanical exhumation and transport of bauxite to a carbonate surface, (2) Al being chemically transported from a weathered crust, or (3) lateritization of aluminosilicate material that has accumulated on carbonate bedrock (Bárdossy, 1982; Combes, 1990). These deposits typically form in the strata directly above recent carbonate platforms on passive margins (Mondillo et al., 2020). Al-rich silicates and hydroxides transported from an adjacent terrigenous source and subsequently infilling the karstified surface characterize the allochthonous origin of these bauxites (Mameli et al., 2007; Torró et al., 2007). Combes (1990) hypothesized that in some cases, this infilling material could be lateritic bauxite, which has been eroded, transported, and deposited on the karstified surface and subjected to *in situ* alterations. The nature of the karst processes and the subsequent mineralogic composition divides karst bauxites into six types: Mediterranean, Timan, Kazakhstan, Ariége, Salento, and Tulsk (Table 1; Bárdossy, 1982).

Sedimentary bauxites represent a third genetic group and form as a result of surficial flows mechanically washing out lateritic bauxites (Bogatyrev et al., 2009). This precedes an

accumulation of clastics on the slopes and foothills of plateaus and rises, characterizing deluvial (valley slope) to proluvial (valley foot) facies or alluvial (ravine-gully) to ephemeral streamflow facies on rare occasions (Bogatyrev et al., 2009). Nodular and colloform (oolites and pisoliths) textures are abundant and indicate the transfer of Al, Fe, and Ti from upper portions of lateritic bodies and subsequent deposition on the surface or within pores and cavities (Bogatyrev et al., 2009). Some sedimentary bauxites form through postsedimentary processes or secondary lateritization (Tsekhovsky, 1987; Tsekhovsky et al., 2008). Subaerial diagenesis (exodiagenesis) is an essential component of secondary lateritization and can result in a kaolinitic clay protolith or primary clastic ore refinement (Tsekhovsky, 1987; Tsekhovsky et al., 2008).

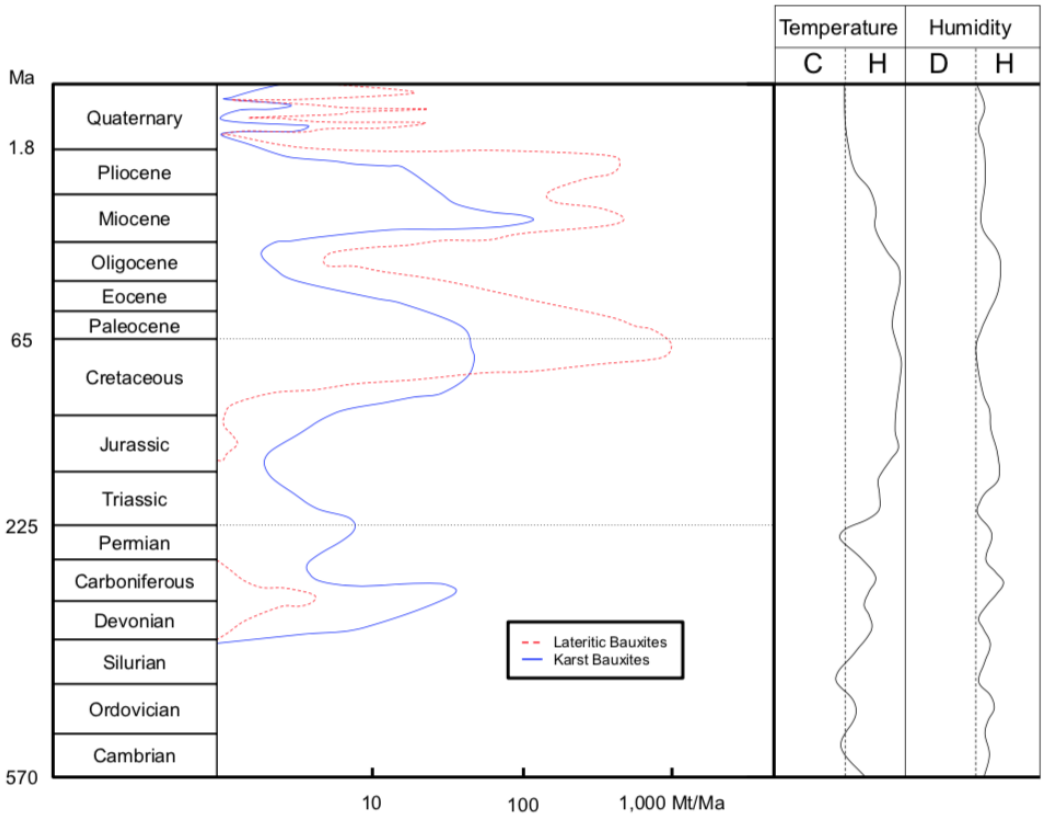

Figure 2. The distribution of lateritic and karst bauxites through time. Temperature: C = Cold, H = Hot; Humidity: D = Dry, H = Humid. Modified from Mondillo et al. (2020) and Bogatyrev et al. (2009).

Bauxite is an important proxy for the typical accumulation of weathered continental crust and paleoclimatic reconstruction (Valeton, 1972; Price et al., 1997). Bauxite records various climatic, biological, and pedogenic environmental conditions, and, as a result, its presence has been used to test the validity of paleoclimatic maps and models (Bárdossy and Aleva, 1990; Price et al., 1997; Bárdossy and Combes, 1999; Valeton, 1999). In terms of climate, bauxite is usually indicative of humid, high precipitation, and high-temperature paleoclimate (Fig. 2; Akayemov et al., 1975; Tardy et al., 1991). Geographically, bauxites are common within tropical to subtropical latitudes in coastal regions (Mondillo et al., 2020). Bauxites postulated to have formed in a wet and cool to cold climate exist and have led to the hypothesis that an alternative geological agent, i.e., the activity of microorganisms, could also cause elements to mobilize during bauxitization (Bucher, 1921; Zajic, 1969; Taylor et al., 1990; Bird and Chivas, 1993; Natarajan et al., 1997; Ehrlich, 2002).

Bauxite and the byproduct of its refinement (red mud) are the most significant global sources of Al_2O_3 and Ga, respectively (Gibson and Hayes, 2011; Frenzel et al., 2016). Al_2O_3 is abundant in the Earth's crust, however, it is mostly concentrated in its ore, bauxite. As a lightweight metal, Al serves many uses in society, such as for consumer products and infrastructure. Gallium is less concentrated in Earth's crust (< 19 mg/kg), and thus no primary mines exist (Ujaczki et al., 2019). Because Ga is present in bauxite in only trace amounts (<50 ppm), it is extracted from red mud (United States Department of Energy, 2010). Gallium-containing compounds such as gallium arsenide (GaAs), gallium nitride (GaN), and copper-indium-gallium selenide ($CuIn_{(1-x)}Ga_{(x)}Se_2$) are semiconductive materials and serve an essential role in the production of microelectronic components, the demand for which has increased in past decades (Foley et al., 2017; Foley et al., 2013). Bauxite is also a potential

source of REEs, including scandium (Sc) (Reid et al., 2017). One of the most well-researched REEs, Sc, is also extracted from red mud (Ochsenkühn-Petropulu et al., 1994). Shaoquan and Suqing (1996) considered ore with Sc concentrations between 0.0002-0.0005% (20-50 mg/kg) to be economically essential resources that warrant full exploitation. Consequently, Binnemans et al. (2013) attributed over 90% of the trace metal value in red mud to Sc.

Geologic Setting

The Mississippi Embayment (ME) is a broad, elongate, and southwest-plunging sedimentary basin and extension of the Gulf of Mexico (GOM) coastal plain that began expressing its modern geography during the Late Cretaceous (100.5-66 Ma) (Murray, 1961; Cushing, 1964). The Laramide Orogeny occurred simultaneously, producing the Rocky Mountains in the area that was once the North American Western Interior Seaway and shed large quantities of sediment to the ME. Marine and deltaic Upper Cretaceous (Cenomanian; 100.5-93.9 Ma) to Upper Eocene (Priabonian; 37.8-33.9 Ma) sediments filled the trough (Stearns, 1957; Autin et al., 1991; Hosman and Weiss, 1991). Pliocene (Piacenzian; 3.6-2.58 Ma) to Quaternary fluvial deposits originating from the Mississippi River and its tributaries locally overlie this fill (Stearns, 1957; Autin et al., 1991; Hosman and Weiss, 1991).

Sediment supply rate to the GOM throughout the Cenozoic varied widely and can be described using 18 chronologically significant depositional episodes (deposodes) (Fig. 3; Galloway et al., 2000). The most pronounced increase in sediment supply to the GOM occurred during the Paleocene. A period of relative sediment starvation began in the early Paleocene and lasted ~3 Ma. The deposition of the thin marine mud-dominated Midway Group defined this time and preceded an abrupt shift occurring during the late Paleocene at the onset of the

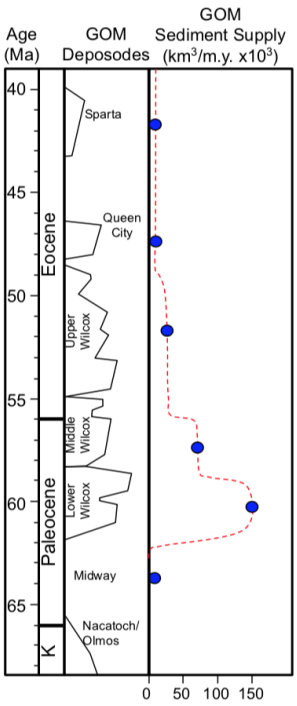

Figure 3. Depositional episodes and sediment supply to GOM sediment routing occurring from the Late Cretaceous to the late Eocene. Modified from Sharman et al. (2017).

sand-rich sediment of the Lower Wilcox deposode (Galloway et al., 2011). The grain volume rate exceeded ~150,000 km^3/Ma, the highest value observed in any multi-million-year deposode (Galloway et al., 2011).

The Midway and Wilcox Groups exhibit a fluvial-deltaic sequence prograding into an arm of the ME (Dupplantis, 1975). Deltaic deposits overlying thin carbonates and thick muds of the Lower Midway are consistent with a steady continental transgression. It was initially hypothesized that the Midway-Wilcox contact represented a regional unconformity based on the sparse occurrence of bauxite (Mellen, 1939). This was refuted by evidence that supports a hypothesis of localized unconformities, which were likely the result of storm surges, splays, and channel incisions (Dupplantis, 1975).

Bauxite orebodies of Late Cretaceous, and early Paleogene age are present in the Gulf Coastal Plain as well as Ridge and Valley regions of the Southeastern United States (Fig. 4).

Four historically recognized bauxite outcrop belts occur in the (1) Cretaceous (contained in Cambrian carbonate bedrock) of AL, GA, TN, and VA; (2) Cretaceous of GA, AL, MS, and TN; (3) Paleocene of MS, AL, and GA; and (4) Eocene of Arkansas AR and MO (Gordon et al., 1958). Of these, the Pulaski-Saline in AR, Eufaula in AL, and Hall-Veneer in GA garner the most attention and have the longest histories of mining activity. Mississippi bauxites are unique among those within the southeastern United States and the world. Deposits are associated with 60-90 m of clays and underlie feldspar-poor fluvio-deltaic sediment. Sediment source locations were likely dominated by limestones, muds, sands, and marls (Thompson, 1981). Bauxitic material (bauxite or bauxitic clay) is present within the Upper Midway and Lower Wilcox Groups, the boundary of which is exposed throughout much of MS (Fig. 5). In MS, the Naheola Fm of the Midway Group, as well as the Nanafalia Fm of the Wilcox Group, contain bauxitic

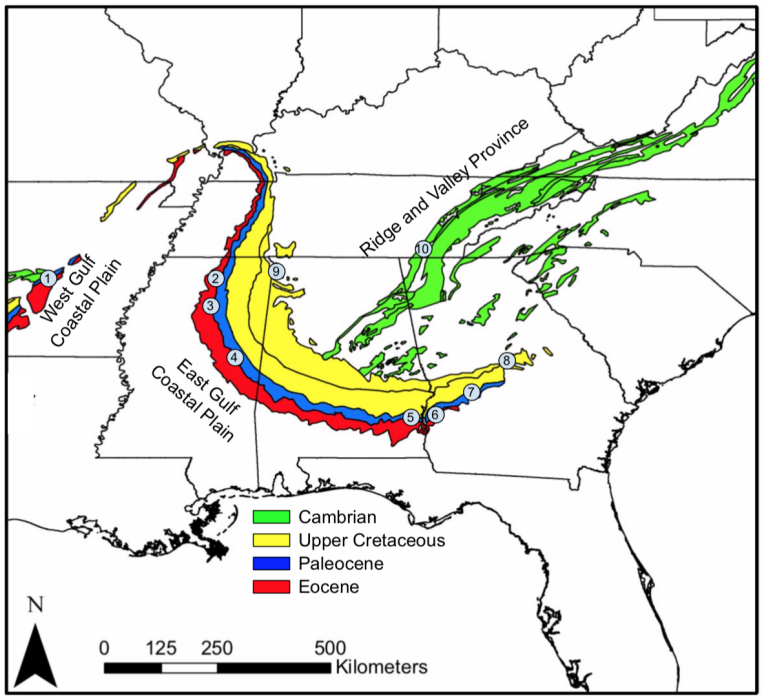

Figure 4. Geographic distribution of bauxite mining districts within the Southeastern United States and associated strata. 1 = Pulaski-Saline District, AR; 2 = Tippah-Benton District, MS; 3 = Pontotoc District, MS; 4 = Winston-Noxubee-Kemper District; 5 = Eufaula District, AL; 6 = Springvale District, GA; 7 = Andersonville, GA; 8 = Irvington, GA; 9 = Margerum District, AL; 10 = Chattanooga District, TN. Modified from (Gordon, 1958).

material. The Coal Bluff and Oak Hill Mbrs, as well as the Gravel Creek Sand and Grampian Hills Mbrs, make up the Naheola Fm and Nanafalia Fm, respectively. Bauxite or bauxitic material is present within the Coal Bluff and Gravel Creek Sand Mbrs (Thompson, 1995).

A white to dark gray carbonaceous clay with silt and fine sand interlaminations and interbeds dominates the Oak Hill Mbr of the Naheola Fm, which conformably overlies the Porters Creek Fm, a grayish-black massive clay. The Oak Hill Lignite defines an upper lignitic zone, which can be useful when correlating strata (Thompson, 1995). The Oak Hill Mbr is ~52 m thick and unconformably underlies the Coal Bluff Mbr of the Naheola Fm. Sands, silts, and clays dominate the Coal Bluff Mbr (Coal Bluff Marl Mbr in AL) of the Naheola Fm. The Coal Bluff Mbr is ~21 m thick and unconformably underlies the Gravel Creek Sand Mbr of the Nanafalia Fm. It contains a distinct bedded kaolinite to bauxitic clay lithofacies also sparsely present in the uppermost Oak Hill Mbr below the basal sands of the Coal Bluff (Thompson, 1995). Mellen (1939) named the kaolinitic to bauxitic clay lithofacies the Betheden Fm or

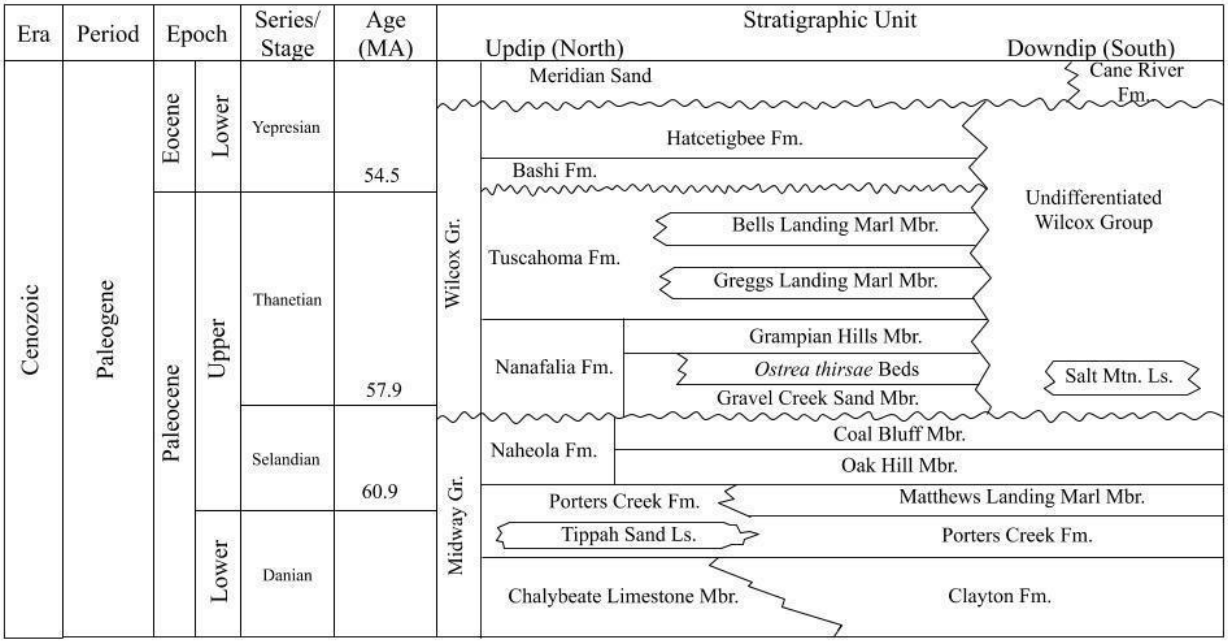

Figure 5. Early Paleogene stratigraphy of Mississippi. Modified from Dockery (1996).

Betheden Residuum, which is now obsolete and argued that residual processes (weathering of soil horizons) at the top of the Midway Group produced the clays (Conant, 1948; MacNeil, 1951; Thompson, 1981). In addition to bedded kaolinite and bauxitic clays, lignite seams typically measuring less than 30 cm in thickness and occurring within the upper two-thirds of the Coal Bluff are useful when correlating strata (Thompson, 1995).

Sands, silts, and clays dominate the Gravel Creek Sand Mbr of the Nanafalia Fm. A section of the Gravel Creek Sand Mbr in East-Central MS will typically exhibit a 21-24-m-thick, white to reddish-orange, fine- to very coarse-grained crossbedded sand interval, as well as a 6-9-m-thick interval of gray, interbedded to interlaminated clays, silts, and sand with sparse beds of lignite (Thompson, 1995). Thompson (1995) interpreted the depositional environment that produced the Gravel Creek Sand Mbr in MS as an incised valley fill underlying a progradational deltaic succession.

Economic Resources

The stratigraphic position of the north MS deposits makes them unique among bauxites in both the southeastern United States and the world, and has made the determination of a genetic history complex (Thompson, 1981). Nearby deposits, Pulaski-Saline in AR and the Eufaula in AL, are both within the Midway-Wilcox interval and are lateritic and karst, respectively. Despite being within the same discontinuous outcrop belt as the Eufaula deposits, those in MS overlie neither an igneous saprolith, nor a karstified carbonate surface and therefore do not represent a typical deposit (Thompson, 1981).

The United States Geological Survey (USGS) has designated mineral commodities as critical; the United States is in a state of reliance on foreign producers (McCullough and Nassar, 2017; Fortier et al., 2018). The United States' reliance on China for its supply of REEs has been

ever-increasing since 1990 (Haxel et al., 2002). Consequently, most of the United States' domestic supply comes from one source: the Mountain Pass Mine in the Mojave Desert, California. Due to 2018 tariffs imposed on Al and steel imports, domestic development of bauxite resources may intensify (Van Gosen and Choate, 2019). The price of REEs and rare earth oxides increased from $300 to $3,600 per kg between the years 2010 and 2011 (United States Environmental Protection Agency, 2012). Van Gosen and Choate (2019) found that despite being the most extensive and pure bauxite deposits in the United States, central AR bauxites lack a significant concentration of critical trace elements and REEs. North MS bauxites are not characterized by a sufficient Al grade to warrant large-scale mining, however, no information regarding trace and REE composition exists (Thompson, 1981). Therefore, this study will provide important information regarding potential economic value of north MS bauxites as a possible source of critical trace elements and REEs.

2. METHODS

Study Area

The study area is located in east-central, north-central, and northeastern MS, USA and is enclosed by a rectangle with corners defined by the coordinates: 34.8°N, 89.3°W and 33.3°N, 89.0°W (Fig. 6). Field sites are located within Pontotoc, Tippah, and Oktibbeha Counties.

Scanning Electron Microscopy

A JSM-7200F Field Emission Scanning Electron Microscope (SEM), along with an Oxford Instruments X-Max^N 80 Energy Dispersive Spectroscopy (EDS) at the University of Mississippi (UM), was used to determine the mineralogy and elemental chemistry of select samples. SEM-EDS was also used to determine pisolith morphology, the extent of cortex development, as well as matrix and cortex major element geochemistry (e.g., Al, Si, Fe, Ti).

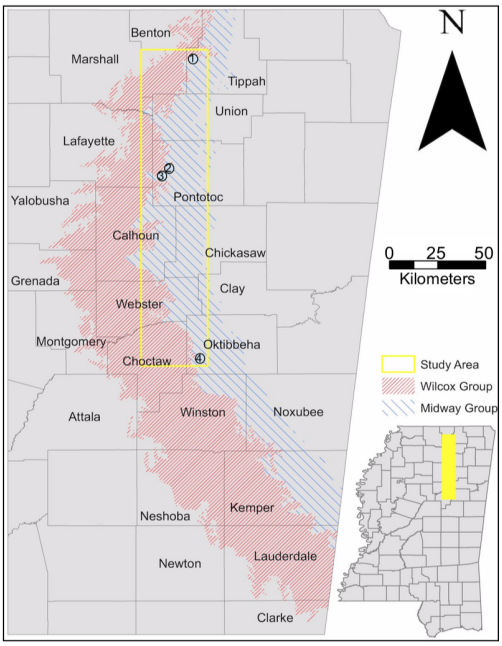

Figure 6. A map of the study area showing the locations where the Midway or Wilcox Group is exposed at the surface. Localities: 1 = Shady Grove; 2 = Third Hill; 3 = Arrow Road; 4 = Sturgis.

Sample Powdering

A Rocklabs Bench Top Ring Mill was used to powder samples. Metal and rubber components of the puck mill were sterilized with acetone and distilled water, respectively prior to each use. The mill was primed with a sample and sterilized a second time prior to sample collection.

Loss-on-Ignition

A Cole Parmer Box Furnace at UM sequentially baked powdered samples in ceramic crucibles at the following increments representing dehydration, combustion of organic carbon, and evolution of carbonate to carbon dioxide, respectively: 24 hours at 105°C, 4 hours at 550°C, and 2 hours at 950°C (Heiri et al., 2001). Mass was recorded before and after each ignition (once cooled in oven to 30°C) and percent loss-on-ignition (LOI) was calculated using the following equations:

$$LOI_{550} = ((Mass_{105} - Mass_{550})/Mass_{105})*100 \quad \text{Eq. 1}$$

$$LOI_{950} = ((Mass_{550} - Mass_{950})/Mass_{60})*100 \quad \text{Eq. 2}$$

$$LOI_{total} = ((Mass_{950} - Mass_{105})/Mass_{105})*100 \quad \text{Eq. 3}$$

X-Ray Diffraction (XRD)

Prior to the analysis of bulk, chemically-treated bulk, and clay mineralogy using a Rigaku MiniFlex X-ray Diffractometer at UM, powdered samples were sieved to 45 μm. Bulk samples were run at 5°/minute, 40 kV, 15 mA, and 30 RPM, while chemically-treated samples and the clay fraction were run at 1°/minute, 40 kV, 15 mA, and 30 RPM.

Chemical treatment used hydrochloric acid (HCl), hydrogen peroxide (H_2O_2), citrate-dithionite (CD) to remove carbonate and soluble organic matter, insoluble organic matter, and iron oxides, respectively. After each treatment, the supernatant liquid was decanted and

discarded and the samples were washed with two successive 40 mL aliquots of distilled water. 1-3 grams were treated for a period of 24 hours with 20 mL of 0.5 M HCl. The residue was treated with 20 mL aliquots of 3.0% H_2O_2 for three successive 24-hour intervals at which point vigorous bubbling had subsided. Samples were then treated for a period of three days with two successive 40 mL aliquots of a 0.3 M sodium citrate and 0.1 M sodium dithionite CD solution (timed 18 hours apart).

In order to separate particles finer than 1.5 μm, chemically-treated samples and 40 mL of distilled water were centrifuged twice at 1500 RPM on an IEC floor centrifuge for 2 minutes and 30 seconds calculated using the equation found in (Jackson, 1979**)**. The pipette method was used in order to mount suspended particles samples onto zero-background slides for XRD analysis.

Elemental Analyses

Inductively coupled plasma – optical emission spectrometry (ICP – OES) in combination with inductively coupled plasma – mass spectrometry (ICP – MS) at Bureau Veritas in Vancouver, Canada quantified major, minor, trace, and REE compositions of powdered samples within a precision of 10-15%. Prior to analysis, powdered samples were sieved to 150 μm at UM and digested using a lithium metaborate/tetraborate flux at Bureau Veritas. Gold (Au) and volatile elements (e.g., copper, nickel, etc.) were digested using Aqua Regia, a method by which a partial digestion is completed using nitric and hydrochloric acid. Additionally, total C and S were determined using the LECO method.

Isotopic Analyses

Prior to isotopic analyses, samples were sieved to between 300 and 250 μm. A ThermoFinnigan MAT 253 Isotope Ratio – Mass Spectrometer (IR – MS) at Southern Methodist University (SMU) measured the oxygen ($\delta^{18}O$) and hydrogen (δD) isotope ratios of carbon

dioxide (CO_2) and hydrogen (H_2) gas, from 12 kaolinitic samples. Precisions for CO_2 and H_2 were 0.1‰ and 2‰, respectively. Standard Mean Ocean Water (SMOW) served as the standard for $\delta^{18}O$ and δD. An Elementar Isoprime100 IR – MS at SMU was used to measure the carbon ($\delta^{13}C$) ratios in the same 12 samples with a precision of 0.1‰. Vienna Peedee Belemnite (VPBD) was used as the standard for calculating $\delta^{13}C$.

3. RESULTS

Field Results

Pontotoc County

The Arrow Road locality, referred to as Randolph Road Metal Pit by Thompson (1981), is a well-exposed outcrop of bauxite in north Mississippi and is located ~2.4 km northwest of Randolph in Pontotoc County at 34.21°N 89.18°W. Because of the thickness of the outcrop, I use this location exclusively for analyses that rely on stratigraphic control for interpretation. I recognize five lithofacies: a lower pisolithic clay, a kaolin interval, mottled clays, friable bauxite, and indurated bauxite (Fig. 7). The first 1.3 m of the section comprises a clay-rich pisolithic zone with a greenish-white color. A white to light tan kaolinitic layer dominates the overlying 1.2 m and transitions into mottled yellowish-white clays, which measures 1 m thick. Above is a thin-layer of friable light yellow bauxite that is 0.4 m thick; it exhibits sharp contacts with underlying and overlying strata as well as cross lamination and pisolihtic texture (Fig. 8). A massive dark yellow bauxite with a pisolithic texture and iron staining comprises the remaining 2.6 m of the section. A sample collected from the uppermost bauxite layer contained several vertically-oriented linear structures ~1 mm in width and ~1-5 cm in length (Fig. 9). These structures are light tan and penetrate through an apparent iron-filled fracture as well as pisoliths, which appear throughout the sample. Pisoliths vary in color between white, dark red, light yellow, or dark green and most have a dark red outer rind.

Three bauxite-bearing localities are near the intersection of Big Hill Road and McDonald Road, which is 7.7 km east of Toccopola, MS. Third Hill is the most well-exposed of the three

and is located 790 m southwest of the intersection (34.26°N 89.16°W). A dirt road leading up the hill intermittently exposes strata, but not well enough for a stratigraphic section to be measured. Bauxite has a dark red matrix and contains pisoliths varying in color between white, dark yellow, dark orange, and dark red (Fig. 10).

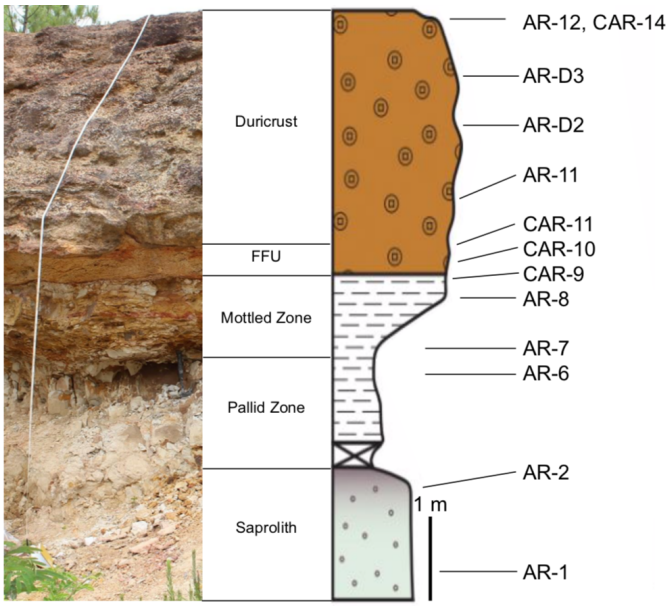

Figure 7. A photograph (left) and section (right) of the Arrow Road outcrop with interpreted lateritic pseudo-horizons (middle), modified from Platt, unpublished data.

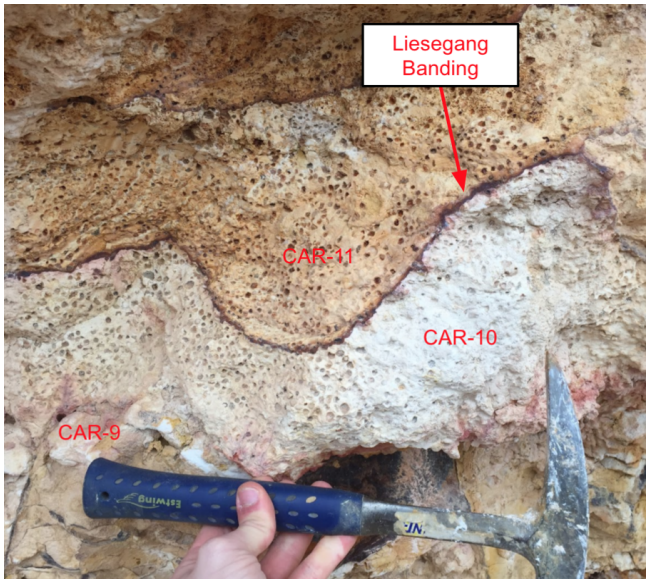

Figure 8. Photographs of the lowermost portion of the upper pisolithic facies at the Arrow Road location in Pontotoc County, MS. Liesegang banding geometry varies from flat to undulatory. Both the lower white and upper yellowish-white units are friable.

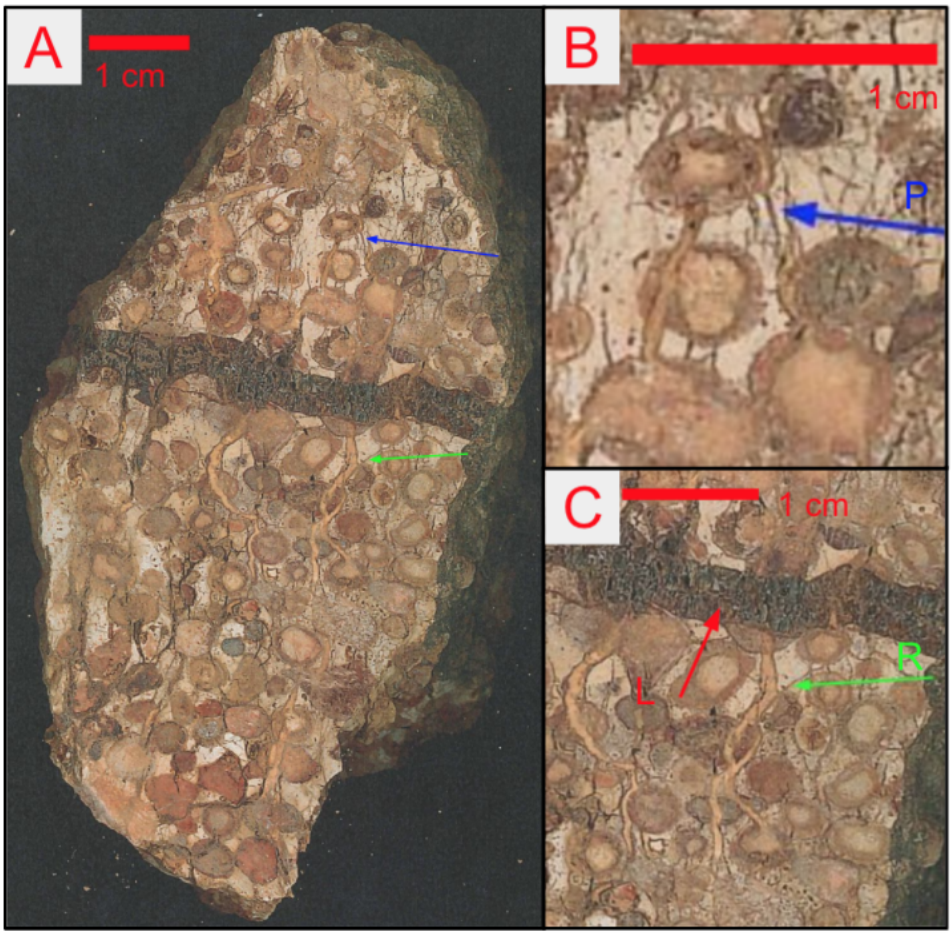

Figure 9. A photograph of sample CAR-14 showing tube-like structures interpreted as rhizoliths (green arrow; R); one appears to be penetrating through a pisolith (blue arrow; P). Liesegang banding (red arrow; L) appears to have formed after pisoliths and rhizoliths.

Tippah County

Shady Grove is the only bauxite-bearing location in Tippah County that was visited for this study. It is located 3.5 km east of Gravestown, MS on County Road 422 and 0.8 km east of the intersection with County Road 429 (34.75°N 89.05°W). Strata are poorly exposed in a steep roadside ditch. Indurated bauxite was also found in float. Exposed strata contain between 20 cm of white-gray massive clay, 13 cm of white to yellow mottled pisolithic clay, and 15 cm of massive light pink clay (Fig. 10). Pisoliths and nodules range from 3-20 mm and are exclusively light gray to orangish-brown.

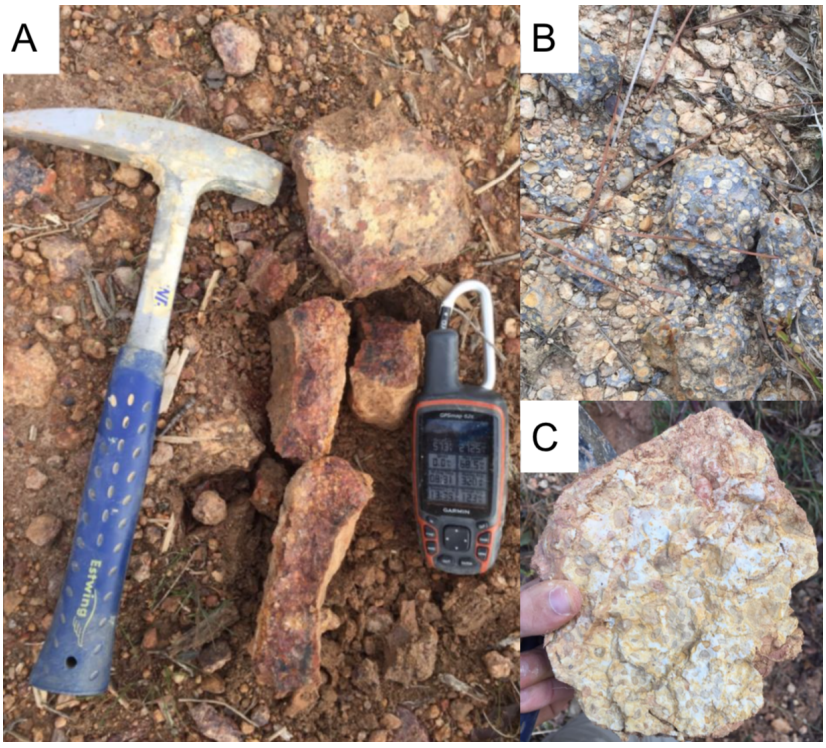

Figure 10. A: A photograph of bauxite from Third Hill. B: A photograph of a pisolithic clay from Shady Grove. Pisoliths measure between 3 and 10 mm, while rare nodules measure between 1 and 2 cm. Float observed at Sturgis locality. Samples are distinctly different from those collected to the north in regards to pisolith composition (clay) and structure (lacking rings) as well as matrix color (blueish gray).

Oktibbeha County

A single sample (ST-1) was collected from a locality ~2.3 km east of the town of Sturgis in Oktibbeha County and 1.3 km past the intersection of Tom Street and Craig Springs Road (33.35°N 89.02°W). Bauxite is exposed on a single horizontal surface and exhibits a blueish-gray silty matrix with light yellow pisoliths with no discernible outer rings (Fig. 10).

XRD Results

The lower pisolithic clay was found to contain kaolinite and siderite. Chlorite was also present however only in sample AR-2 (Appendix 2). The overlying kaolin interpreted as the plasmic zone contained kaolinite, and chlorite. The mottled clay (AR-8) contained muscovite, kaolinite, and goethite. Boehmite was found only within samples CAR-11, AR-11, and AR-D2,

constituting the lower portion of the upper bauxitic zone. The mineralogy of the upper bauxitic zone is characterized by the clay minerals kaolinite and chlorite as well as gibbsite and goethite. The pisolithic clay from the Shady Grove location was found to contain exclusively kaolinite, while the bauxite from Sturgis contained kaolinite, quartz, and gibbsite. The bauxites from Third Hill, samples TH-3 and TH-5, had a mineralogy of kaolinite, boehmite, gibbsite, and goethite.

Scanning Electron Microscopy

Scanning electron microscopy confirmed prior reports of iron-rich nodules in the lower pisolithic clay (Fig. 11). These were contained within a clayey matrix. Sample AR-6 was found to have a homogenous clay-rich composition. AR-8, contained Fe-rich mottles ~0.75 mm in diameter; between these mottles are a clayey matrix (Fig. 11). Sample AR-11, bauxite from the lower portion of the upper bauxitic zone, contained pisoliths that were ~2-4 mm in diameter (Fig. 11). Pisoliths have Al nuclei with cortices rich in Fe. In one case, an Al-rich cortex separated two Fe-rich ones. Additionally, this pisolith had an internal structure defined by an abundance of Al and Ti arranged in a dendritic pattern. Pisoliths occur within a clay matrix. Sample AR-D2 contained a higher concentration of pisoliths and pisolith matrices were dominated by an Al-rich chemistry with rare occurrences of Fe-rich matrices and were 2-4 mm in diameter (Fig. 11). Pisoliths with Al-rich matrices have Fe-rich cortices and have a matrix that is more concentrated in Ti compared to the aluminosilicate matrix. Sample CAR-14, collected from approximately the same elevation as AR-12, contained what is interpreted as a rhizolith, Liesegang banding, and pisoliths (Fig. 12). Pisoliths were 2-6 mm in diameter and had matrices that were characterized by Al and Si chemistry. Additionally, pisolith cortices contained Al, Fe, as well as overlapping Fe and Si (Fig. 12). The interpreted rhizolith contained a slightly higher concentration of Si compared to the surrounding material. Within close proximity to the interpreted rhizolith were

several small tube-like to plate-like carbonaceous structures between 20 μm and 30 μm in length (Fig. 12). A third rope-like structure was observed measuring ~150 μm in length and 3 μm in width before extending into the interior of the sample (Fig. 13).

Sample ST-1 contained an Al- and Si-rich matrix as well as pisoliths ~2 to 3 mm in diameter (Fig. 14). These pisoliths were Al- and Si-rich and lacked any discernible cortices. They do, however, contain an elevated concentration of Ti compared to the matrix. The matrix also contains very fine- to medium-grained sand quartz grains and minor occurrences of Fe further distinguishing the two.

Samples TH-3 and TH-5 were collected from the Third Hill locality. TH-3 contains 2-3 mm diameter Al-rich pisoliths in an Fe-rich matrix (Fig. 14). One pisolith was observed that had an Fe-rich matrix with a single Al-rich cortex. A second pisolith contains a small zonation of Fe within its dominantly Al matrix. Within this Fe-rich zone is a small fracture that has been filled with an Al-rich material. TH-5 contains 2-3 mm in diameter Al-rich pisoliths in an Fe-rich matrix (Fig. 14). TH-3 contains a greater concentration of Si in its matrix compared to TH-5.

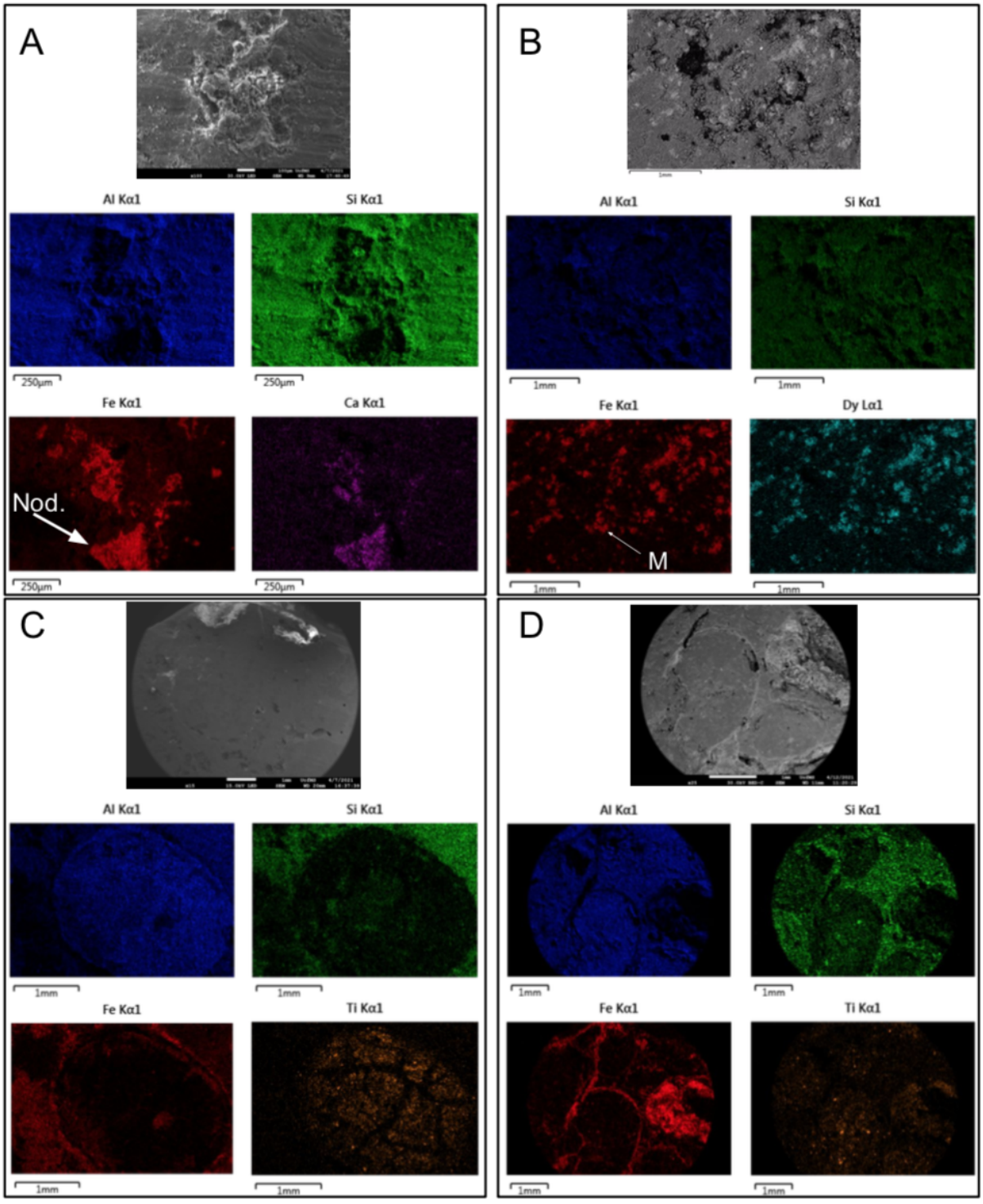

Figure 11. SEM (top) and EDS images (bottom) of samples A = AR-1; B = AR-8; C = AR-11; D = AR-D2. Sample AR-1 exhibits an Fe-rich nodule (Nod.), most likely siderite. This is interpreted as a possible cause for elevated Fe in the lower clays. Sample AR-8 exhibits Fe-rich mottles (M) in an otherwise kaolinitic matrix. Sample AR-11 exhibits a pisolith with multiple discernible cortices and a complex internal structure. Sample AR-D2 showing 6 pisoliths, 5 of which are enriched in Al, 1 in Fe. All have an outer coating rich in Fe.

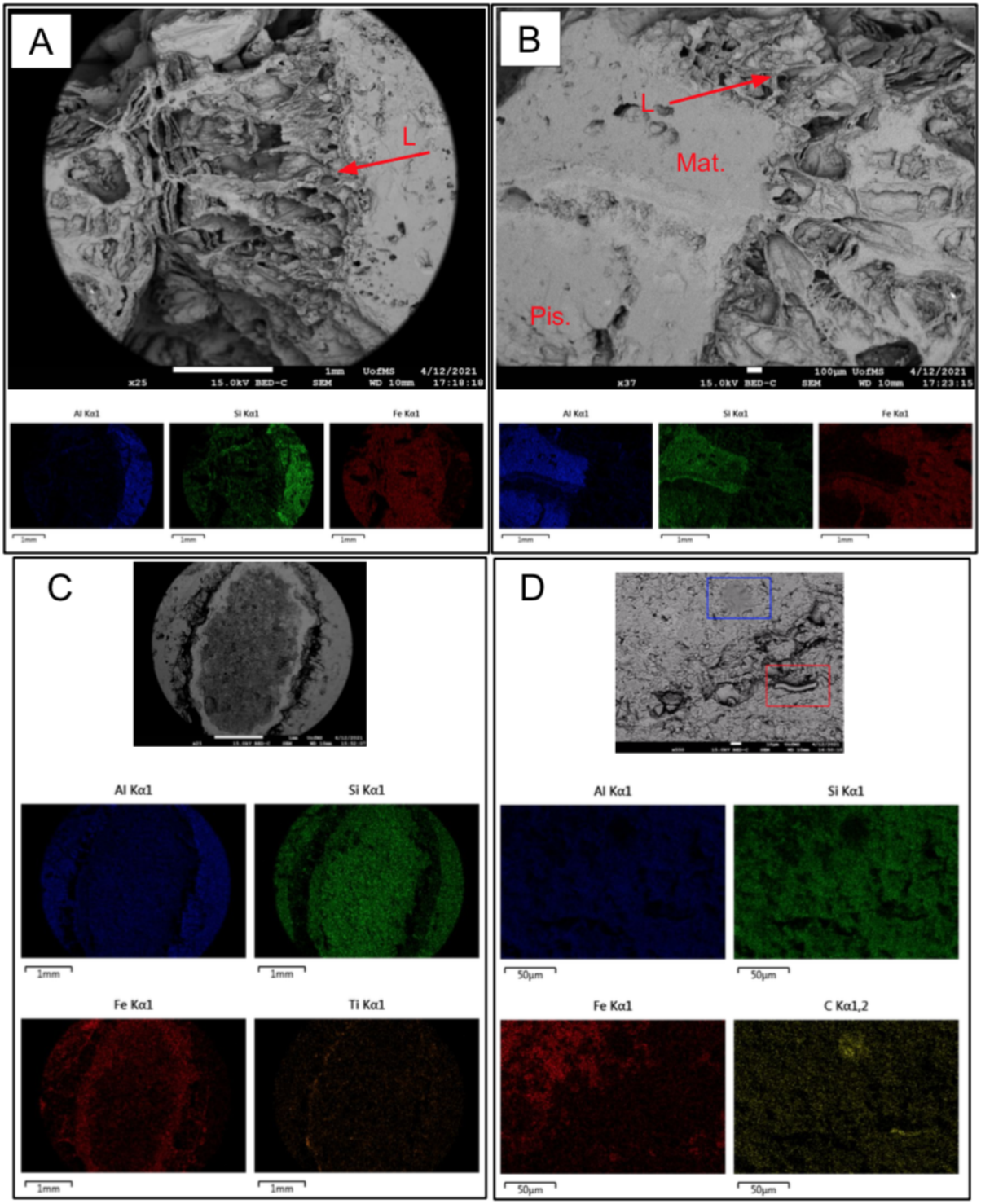

Figure 12. SEM (top) and EDS images (bottom) of sample CAR-14 . A = SEM-EDS image of sample CAR-14 showing Fe-rich Liesegang banding (L) adjacent to the clay-rich matrix. B = SEM-EDS image of sample CAR-14 showing Fe-rich Liesegang banding adjacent to clay-rich matrix (Mat.) as well as a pisolith (Pis.) with Fe- and Al-rich cortices. C = SEM-EDS image of sample CAR-14 showing Fe- and Al-rich cortices surrounding an Al- and Si-rich pisolith. D = SEM-EDS image of sample CAR-14 showing tubular (red box) and plate-like (blue box) carbonaceous structures.

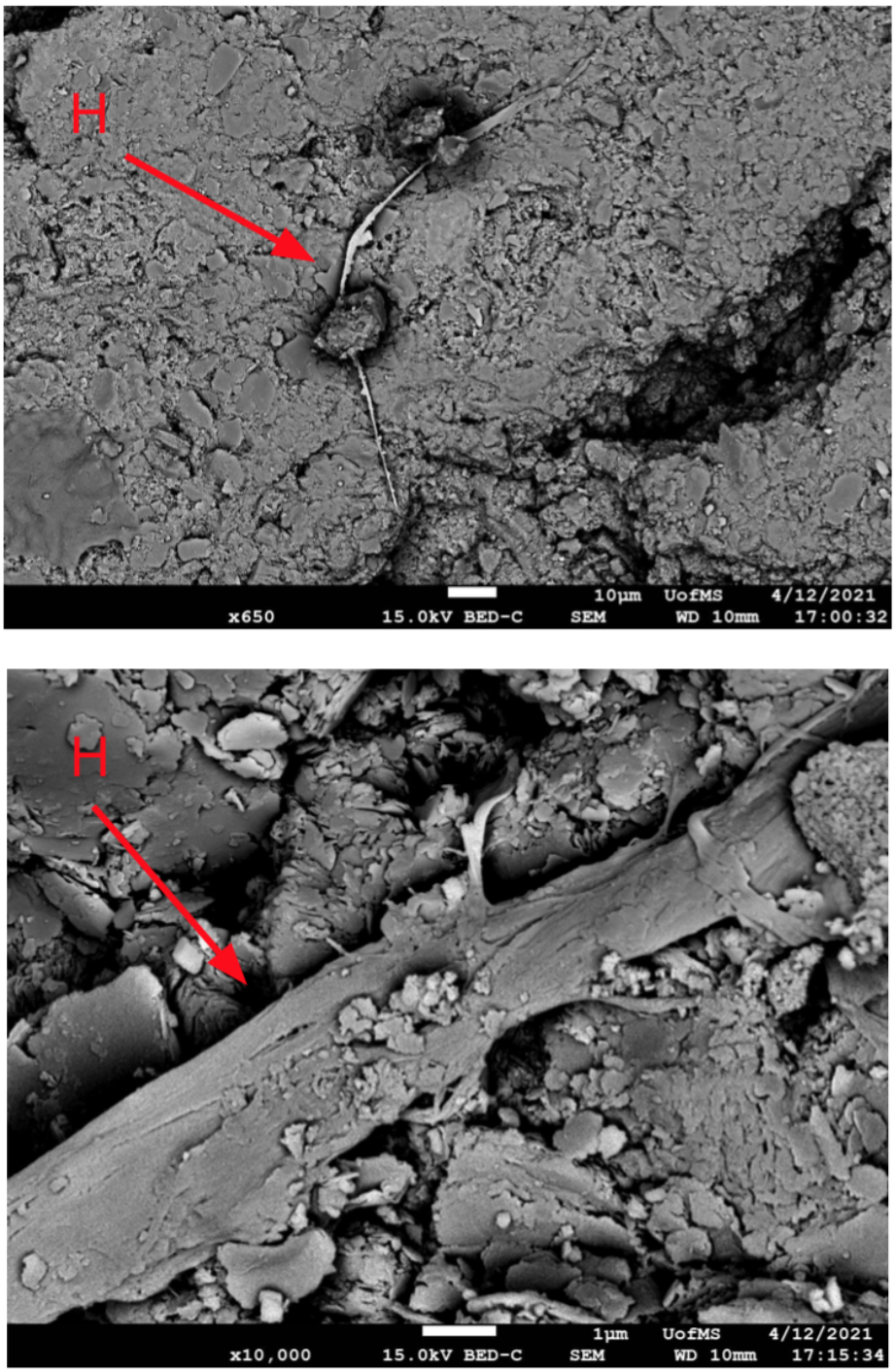

Figure 13. SEM image of a rope-like structure within sample CAR-14 interpreted as a fungal hyphae based on size and morphology.

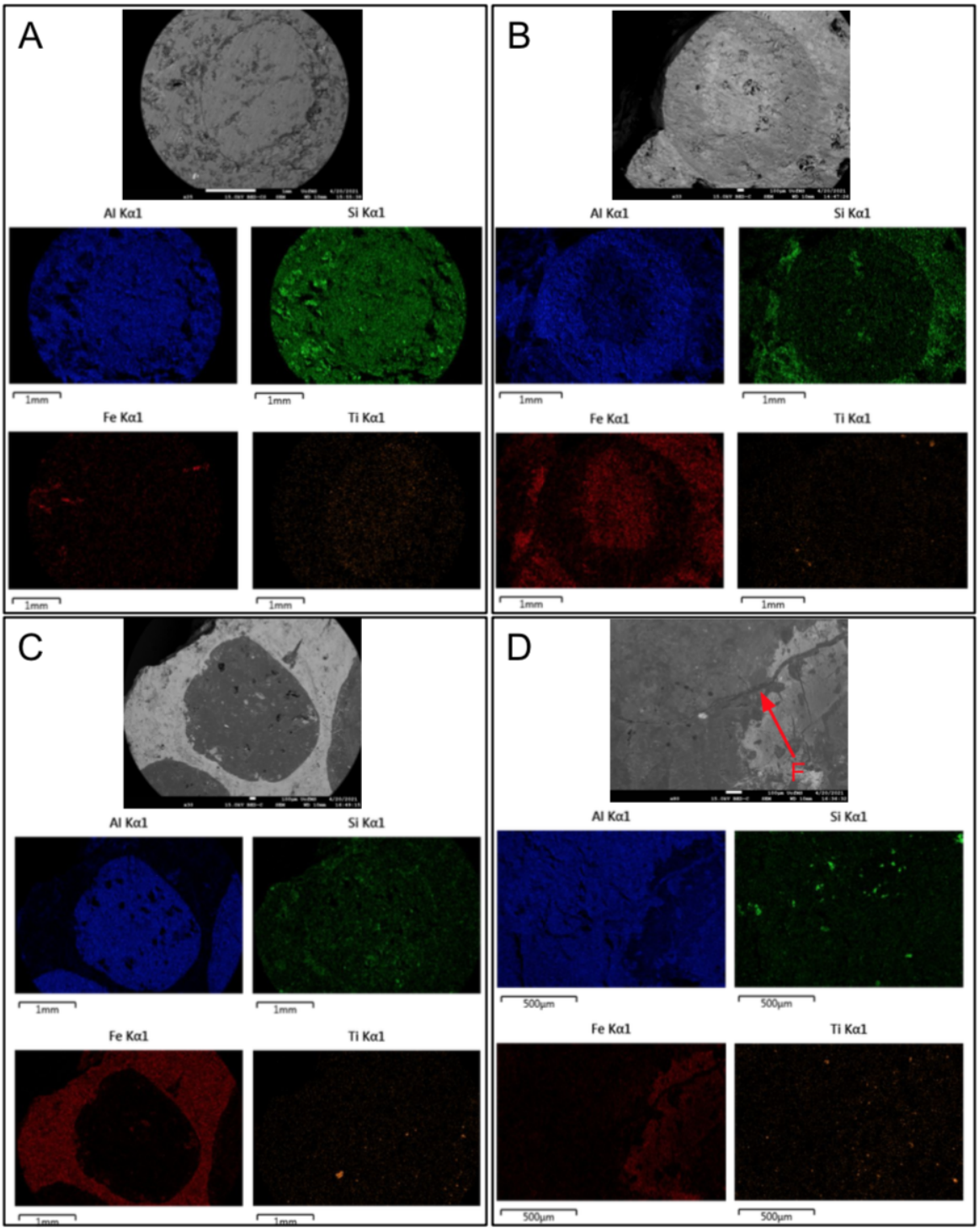

Figure 14. SEM (top) and EDS images (bottom) of samples A = ST-1; B = TH-3; C = TH-5; D = TH-5. A = SEM-EDS image of sample ST-1 showing an Al- and Si-rich pisolith within a Al- and Si-rich matrix with sparse quartz grains. B = SEM-EDS image of sample TH-3 showing an Fe-rich pisolith with an Al-rich cortex within an Fe- and Si- rich matrix. C =: SEM-EDS image of sample TH-5 showing an Al-rich pisolith within an Fe-rich matrix. D = SEM-EDS image of sample TH-5 showing a possible fracture, which has been filled by an Al-rich mineral.

Elemental Geochemistry

Major Element Geochemistry

Major oxide compositions for 15 bauxite and associated clay samples were obtained using ICP-OES and are shown in Table 2. At the main Arrow Road outcrop, samples analyzed had an Al_2O_3 composition ranging from 16.41% in the upper bauxitic zone to 42.86% in the lower clayey zone, however it did not noticeably increase or decrease going upsection (Fig. 15). Fe_2O_3 ranged from 0.54% in the lower clayey zone to 59.18% in the upper bauxitic zone and generally increased upsection. SiO_2 ranged from 6.47% in the upper bauxitic zone to 43.29% in the lower pisolithic clay and generally decreased upsection. Between samples AR-2-1 and AR-2-3, Al_2O_3 increased from 40.86% to 44.52%, SiO_2 decreased from 31.82% to 14.22%, and Fe_2O_3 increased from 0.97% to 13.03%. Between samples CAR-10 and CAR-11, Al_2O_3 decreased from 42.45% to 39.56%, SiO_2 decreased from 31.89% to 30.6%, and Fe_2O_3 increased from 3.98% to 8.45%. Sample ST-1 had the highest SiO_2 composition of any sample at 49.6%, an Al_2O_3 composition of 32.2%, and an Fe_2O_3 composition of 1.9%.

MgO, CaO, and MnO all decreased upsection. TiO_2 decreased upsection as well, albeit to a lesser degree. In addition, Na_2O and K_2O remained low throughout the section, but spiked significantly at the contact of the lower clayey zone and the upper bauxitic zone. Cr_2O_3 and P_2O_5 both increased.

Within the Arrow Road bauxites there was a strong positive correlation between TiO_2 and Al_2O_3 ($r^2 = 0.837$; n = 6). There is also a strong positive correlation between SiO_2 and Al_2O_3 as well as a strong negative correlation between Al_2O_3 and Fe_2O_3.

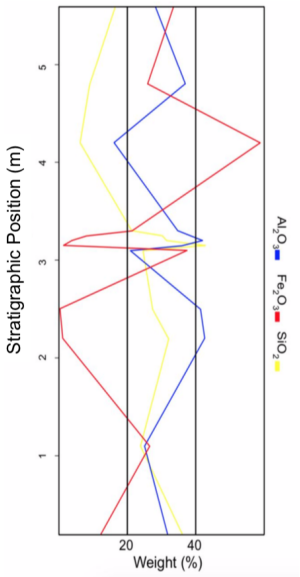

Figure 15. Major oxide weight percentage as a function of stratigraphic position within the Arrow Road section. Fluctuations closely resemble those present within the typical lateritic bauxite profile and reflect processes of illuviation and eluviation.

Table 2. Major oxide compositions (weight %) measured using ICP-OES.

Sample	SiO_2	Al_2O_3	Fe_2O_3	MgO	CaO	Na_2O	K_2O	TiO_2	P_2O_5	MnO	Cr_2O_3
AR-1	36.36	32.01	12.61	0.39	0.38	0.04	0.1	2.15	0.05	0.06	0.033
AR-2	24.19	25.39	26.79	0.72	0.81	0.02	0.06	2.14	0.06	0.14	0.036
AR-6	32.38	42.86	1.41	0.1	0.06	0.03	0.03	3.79	0.04	<0.01	0.039
AR-7	27.71	41.66	0.54	0.09	0.05	0.03	0.01	2.12	0.08	<0.01	0.028
AR-8	24.86	21.18	37.8	0.24	0.04	0.05	0.51	1.55	0.04	0.04	0.02
AR-11	21.66	35.12	21.58	0.03	0.11	0.01	0.08	1.22	0.15	0.01	0.055
AR-12	16.82	28.41	33.87	0.05	0.03	<0.01	0.06	1.2	0.23	0.04	0.044
CAR-9	43.29	36.54	1.62	0.28	0.06	0.09	0.9	3.08	0.04	<0.01	0.04
CAR-10	31.89	42.45	3.98	0.09	0.04	0.06	0.19	1.96	0.08	<0.01	0.07
CAR-11	30.6	39.56	8.45	0.09	0.02	0.26	0.17	1.71	0.11	<0.01	0.059
AR-D2	6.47	16.41	59.18	0.02	0.01	<0.01	0.06	0.77	0.14	0.06	0.03
AR-D3	9.3	37.24	26.31	0.04	0.03	<0.01	0.06	1.88	0.27	0.02	0.058
AR-2-1	31.82	40.86	0.97	0.08	0.05	0.02	0.03	2.85	0.04	<0.01	0.04
AR-2-3	14.22	44.52	13.03	0.04	0.02	<0.01	0.04	2.8	0.13	<0.01	0.04
ST-1	49.6	32.2	1.9	0.04	0.15	<0.01	0.03	0.83	0.76	<0.01	0.029

Lithologic Classification

Samples were classified based on Al_2O_3-Fe_2O_3-SiO_2 composition using the methods of Boulange et al. (1996), Aleva (1994), Bárdossy (1982), Schellman (1986), and Beauvais (1991). The samples from the lower clayey zone at the main Arrow Road outcrop plot within the kaolinite and argillo-ferruginous bauxite fields. Those collected from the area designated as the upper bauxitic zone plot within the argillo-ferruginous bauxite field in the Al_2O_3-Fe_2O_3-SiO_2 ternary diagram according to Boulange et al. (1996; Fig. 16). Both samples from the second Arrow Road outcrop plot within the argillo-ferruginous bauxite field. Sample ST-1 plots within the kaolinite field, despite its bauxite-like texture.

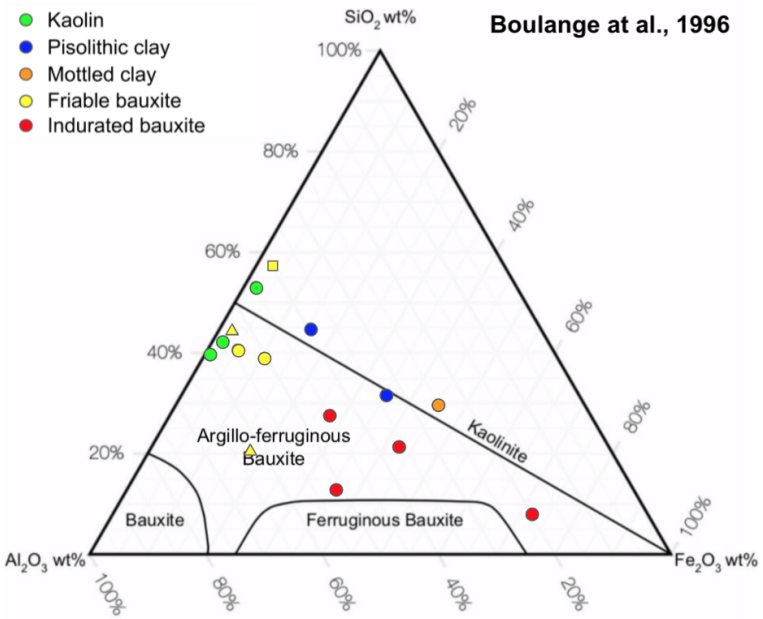

Figure 16. A ternary diagram with accompanying color code (top left) of the SiO_2-Al_2O_3-Fe_2O_3 system (Boulange et al., 1996). Circles denote samples from the main Arrow Road outcrop, triangles denote those from the second outcrop at the Arrow Road location, and the square represents sample ST-1.

Samples from the lower clayey zone at the main Arrow Road outcrop plot within the kaolinite bauxite, bauxite kaolinite, and laterite fields. Samples from the area designated as the upper bauxitic zone plot within the kaolinite bauxite, bauxite, laterite, and bauxite ferrite fields in the Al_2O_3-Fe_2O_3-SiO_2 ternary diagram according to Aleva et al. (1994; Fig. 17). Samples below and above Liesegang banding at the second Arrow Road outcrop plot within the kaolinite bauxite and bauxite fields, respectively. Sample ST-1 plots within the laterite field.

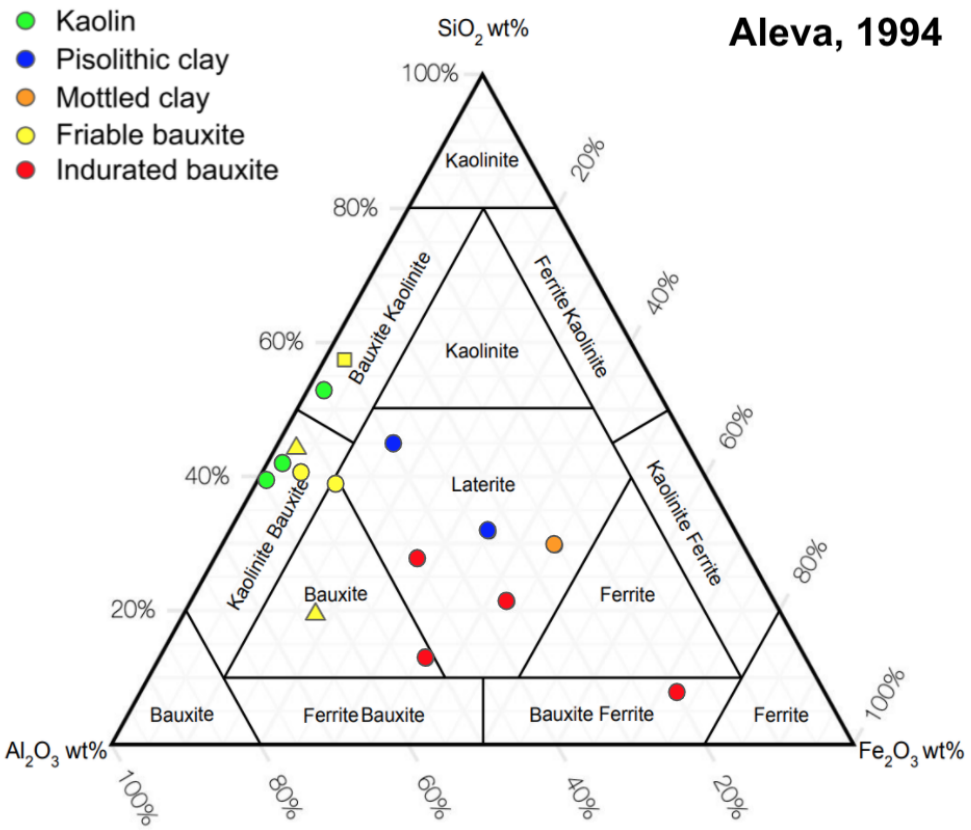

Figure 17. A ternary diagram with accompanying color code (top left) of the SiO_2-Al_2O_3-Fe_2O_3 system (Aleva, 1994). Circles denote samples from the main Arrow Road outcrop, triangles denote those from the second outcrop at the Arrow Road location, and the square represents sample ST-1.

Samples from the lower clayey zone at the main Arrow Road outcrop plot within the bauxitic clay, clayey bauxite, and bauxitic clayey iron ore fields. Samples from the area designated as the upper bauxitic zone plot within the bauxitic iron ore, iron-rich bauxite, and clayey bauxite fields in the Al_2O_3-Fe_2O_3-SiO_2 ternary diagram according to Bárdossy (1982; Fig. 18). Samples below and above Liesegang banding at the second Arrow Road outcrop plot within the clayey bauxite and bauxite sandstone fields respectively. Sample ST-1 plots within the bauxitic clay field.

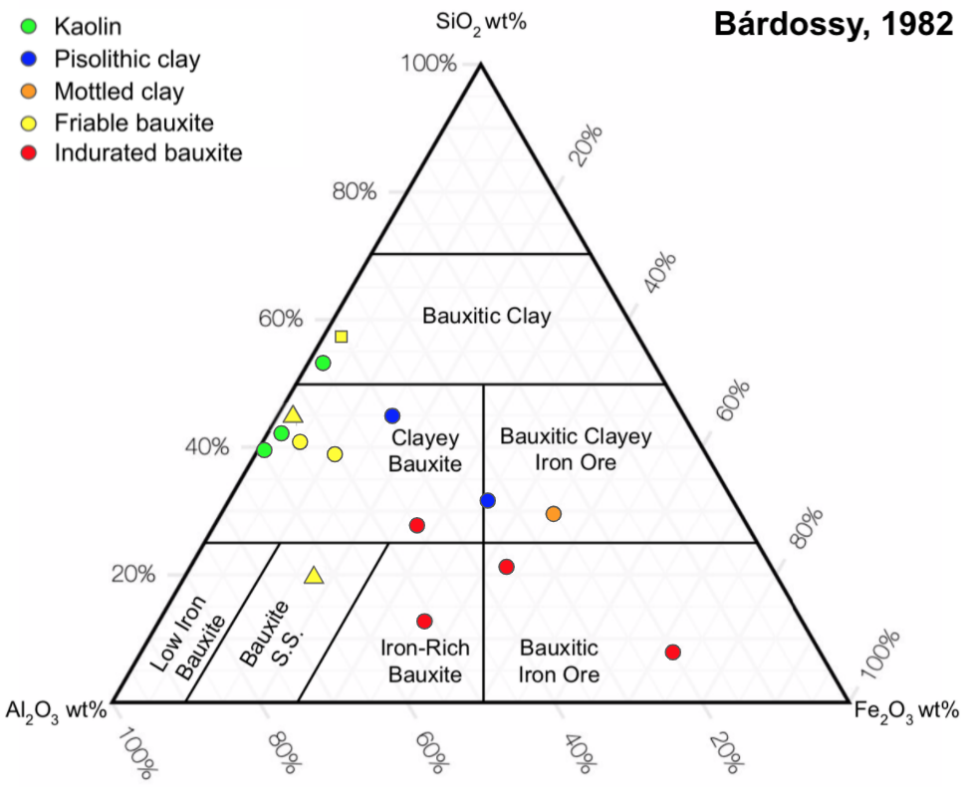

Figure 18. A ternary diagram with accompanying color code (top left) of the SiO_2-Al_2O_3-Fe_2O_3 system (Bárdossy, 1982). S.S. = Sandstone. Circles denote samples from the main Arrow Road outcrop, triangles denote those from the second outcrop at the Arrow Road location, and the square represents sample ST-1.

Degree of Lateritization

Samples from within the lower clayey zone plot within the weak lateritization and moderate lateritization fields (Fig. 19). Samples from the upper bauxitic zone plot within the moderate and strong lateritization fields. Samples below and above Liesegang banding at the second Arrow Road outcrop plot within the moderate and strong lateritization fields respectively. Sample ST-1 plots within the weak lateritization field.

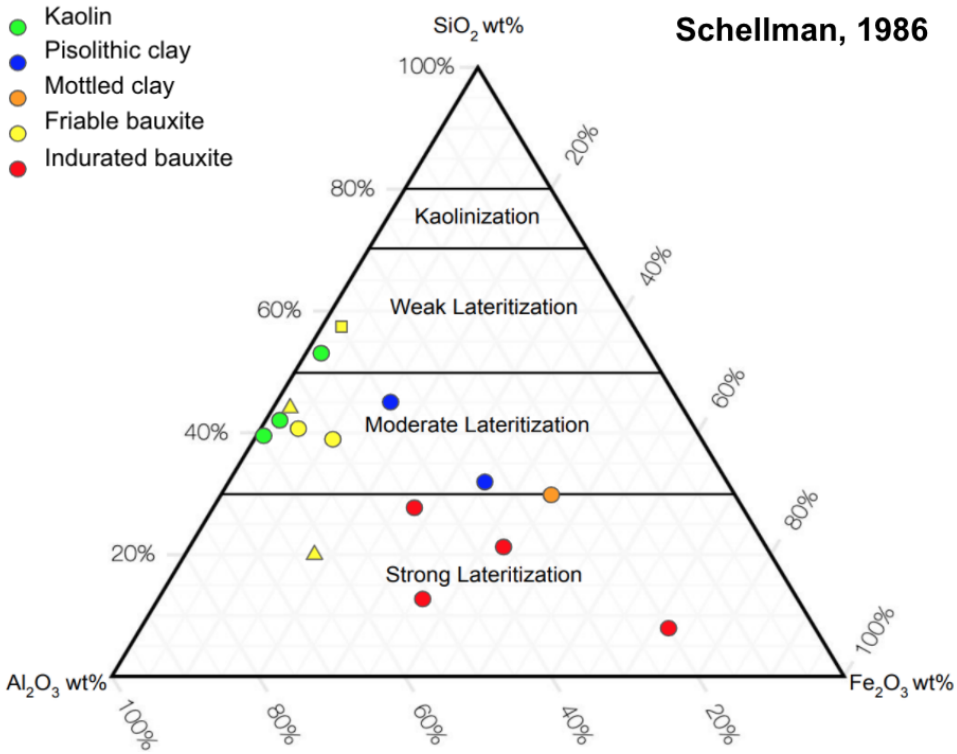

Figure 19. A ternary diagram with accompanying color code (top left) of the SiO_2-Al_2O_3-Fe_2O_3 system showing the varying degrees of lateritization possible (Schellman, 1986). Circles denote samples from the main Arrow Road outcrop, triangles denote those from the second outcrop at the Arrow Road location, and the square represents sample ST-1.

Dismantlement Pathways

Using the Al_2O_3-Fe_2O_3-SiO_2 ternary diagram as described in Beauvais (1991; Fig. 20), it was determined that the dominating dismantlement pathway followed during bauxitization at the Arrow Road outcrop was dehydration. This was most apparent in the sequence of samples CAR-9, CAR-10, CAR-11, AR-11, and AR-D2. The transition from sample AR-D2 to sample AR-D3 is marked by a drop in Fe_2O_3 content. Samples AR-2-1 and AR-2-3 follow a similar trend as CAR-10 and CAR-11, increasing in Fe_2O_3 content.

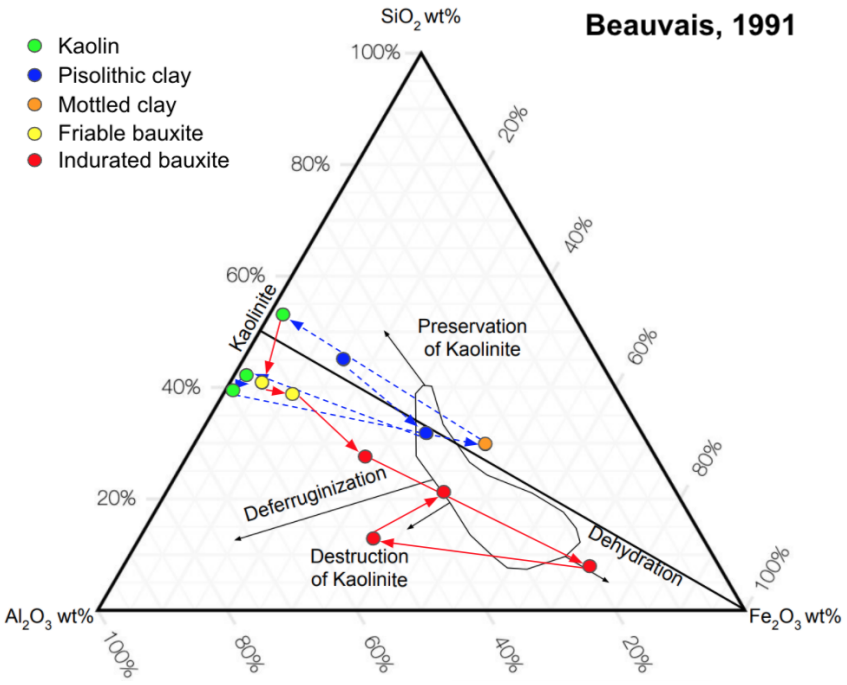

Figure 20. A ternary diagram with accompanying color code (top left) of the SiO_2-Al_2O_3-Fe_2O_3 system showing the possible geochemical dismantlement pathways that may have taken place during bauxitization (Beauvais, 1991). Circles denote samples from the main Arrow Road outcrop, triangles denote those from the second outcrop at the Arrow Road location, and the square represents sample ST-1. Red arrows indicate pathway followed upsection starting at the top of the lower clay-rich zone. Blue arrows indicate pathway followed upsection starting at the base of the lower clay-rich zone through the top of the lower clay-rich zone.

Weathering Indices

Of the 7 weathering indices used to analyze the data, Vogt's Residual Index (V) and Silica-Titania Index (STI) showed the most substantial changes upsection (Table 3-4; Fig. 21). Both followed trends associated with increased weathering going upsection. The Chemical Index of Alteration (CIA), which is commonly used for analyzing bauxite and laterite deposits, showed minimal change going upsection. Both the Chemical Index of Weathering (CIW) and the Plagioclase Index of Alteration (PIA) show the greatest change at the shift from the interpreted saprolite to the lower clay horizon. The Weathering Index of Parker (WIP) showed almost no change going upsection and only a minor spike occurring at the base of the upper bauxitic zone.

Table 3. The chemical weathering indices that were used to determine the extent of weathering among samples (Price and Velbel, 2003).

Index	Formula	Trend With Increased Weathering
R	SiO_2/Al_2O_3	Negative
WIP	$100[(2Na_2O/0.35) + (MgO/0.9) + (2K_2O/0.25) + (CaO/0.7)]$	Negative
V	$(Al_2O_3 + K_2O)/(MgO + CaO + Na_2O)$	Positive
CIA	$100[Al_2O_3/(Al_2O_3 + CaO + Na_2O + K_2O)]$	Positive
CIW	$100[Al_2O_3/(Al_2O_3 + CaO + Na_2O]$	Positive
PIA	$100[(Al_2O_3 - K_2O)/(Al_2O_3 + CaO + Na_2O - K_2O)]$	Positive
STI	$100[(SiO_2/TiO_2)/((SiO_2/TiO_2)+(SiO_2/Al_2O_3)+ (Al_2O_3/TiO_2))]$	Negative

Table 4. Chemical weathering indices calculated for each sample.

Sample	R	WIP	V	CIA	CIW	PIA	STI
AR-1	1.14	200.48	39.64	98.40	98.70	98.70	51.35
AR-2	0.95	255.14	16.42	96.61	96.83	96.83	46.86
AR-6	0.76	60.83	225.74	99.72	99.79	99.79	41.46
AR-7	0.67	42.29	245.12	99.78	99.81	99.81	39.15
AR-8	1.17	468.95	65.73	97.25	99.58	99.57	51.94
AR-11	0.62	88.76	234.67	99.43	99.66	99.66	37.65
AR-12	0.59	57.84	355.88	99.68	99.89	99.89	36.61
CAR-9	1.18	811.11	87.07	97.21	99.59	99.58	51.86
CAR-10	0.75	202.00	224.42	99.32	99.76	99.76	42.06
CAR-11	0.77	297.43	107.38	98.88	99.30	99.29	42.81
AR-D2	0.39	51.65	549.00	99.58	99.94	99.94	27.91
AR-D3	0.25	56.73	532.86	99.76	99.92	99.92	19.78
AR-2-1	0.78	51.46	272.60	99.76	99.83	99.83	42.48
AR-2-3	0.32	39.30	742.67	99.87	99.96	99.96	23.85
ST-1	1.54	49.87	169.63	99.44	99.54	99.54	59.70

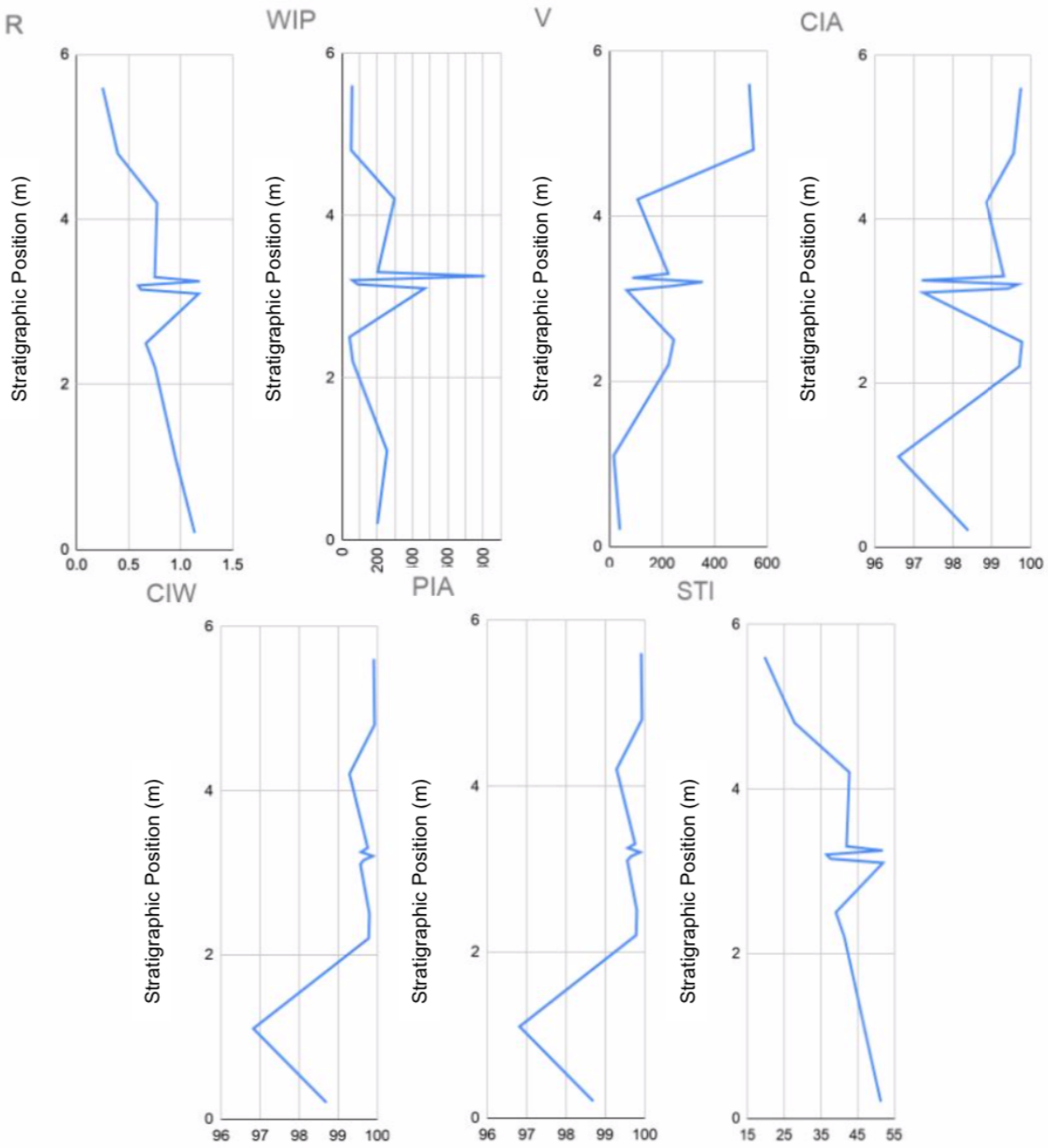

Figure 21. Chemical weathering indices as a function of stratigraphic position at the Arrow Road site.

Trace Element Geochemistry

Trace element compositions for 9 bauxites and 6 associated clay samples from Arrow Road and Sturgis are shown in Tables 5 and 6. Ga concentrations in bauxite at Arrow Road range from 33.1 ppm to 74.2 ppm and remain relatively constant throughout the section. Zr and Nb both decreased upsection, Zr from 1726.9 ppm to 397 ppm and Nb from 70.2 ppm to 13.5 in the lower clayey zone and the upper bauxitic zone, respectively. Ni, Hg, and Sr were generally low throughout the section with the exception of sample AR-8 located immediately below the contact of the lower clayey zone and upper bauxitic zone. In a bivariate plot of Cr and Ni concentrations, all samples plot within the high-Fe lateritic bauxite field (Fig. 22). Zr, Cr(Ni), and Ga abundances plot within the acidic and metamorphic field of a ternary diagram related to bauxite parent material (Fig. 23). There exist strong positive correlations between TiO_2 and high field strength elements (i.e., Zr, Hf, Nb, and Ta) within bauxite samples.

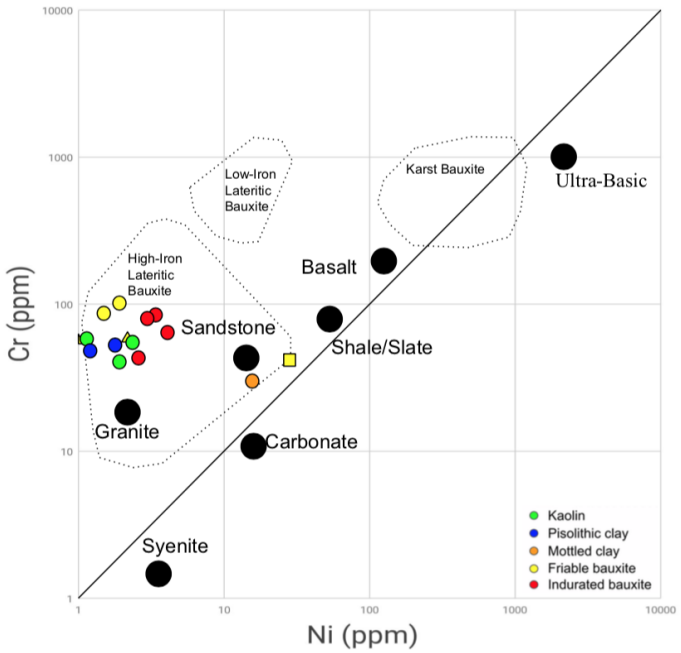

Figure 22. Plot with accompanying color code (bottom right) showing likely bauxite protoliths based on Ni and Cr abundances, based on Schroll and Schauer (1968). Circles denote samples from the main Arrow Road outcrop, triangles denote those from the second outcrop at the Arrow Road location, and the square represents sample ST-1.

Table 5. Trace element compositions (ppm) measured using ICP-MS.

Sample	Ba	Sc	Be	Co	Cs	Ga	Hf	Nb	Rb	Sn	Sr	Ta	Th	U	V	W	Zr	Y
AR-1	55	17	<1	0.9	0.6	56.3	29.6	40	4.5	5	25.6	2.7	26.3	6.3	387	3.1	1165.7	33.9
AR-2	47	21	<1	1	0.5	49.3	30.9	40.4	3.4	5	26.3	2.6	31.3	6.7	499	4.2	1208.4	39.4
AR-6	52	23	2	1.7	0.2	65.6	44.8	70.2	1.7	10	25.3	4.4	45.2	11.3	220	7	1726.9	56.6
AR-7	35	22	<1	1.9	0.1	62.8	15.3	37.5	1	6	19.9	2.4	25.6	8.2	214	4.2	589.7	23.6
AR-8	196	27	<1	2.5	1.4	29.3	18.3	29.1	20.1	4	34	1.9	18.3	4.9	294	2.5	680.6	29.4
AR-11	40	19	<1	1.3	0.5	45.9	17.7	22.4	4.2	4	10.2	1.3	38.5	4.6	549	2.2	666	18.8
AR-12	73	17	<1	3.6	0.3	46.6	16.4	21	3.7	3	172.8	1.4	34.2	3.6	605	2.6	616.6	17.9
CAR-9	321	17	2	2.3	2.1	44.3	45.1	53.4	33	6	54.2	3.5	32.8	8.4	348	4.3	1703.9	57.7
CAR-10	76	17	1	1.1	0.8	51.7	29.3	33.7	8.4	5	20.2	2.3	50	8.3	674	2.4	1071.5	28.8
CAR-11	67	19	1	1	0.6	49.3	24.6	29.4	7.2	5	14.3	2	45.3	6.2	722	2.6	894.3	26.2
AR-D2	37	21	1	1.8	0.3	33.1	10.7	13.5	3.1	2	7.4	0.9	21.7	2.5	494	1.7	397	12.6
AR-D3	52	19	<1	1.8	0.6	74.2	24.8	32.3	3.6	5	17.9	2.2	47.8	5	620	3.8	926.2	29
AR-2-1	45	15	<1	0.9	0.3	68.5	36	51.1	2.1	7	23	3.5	39.3	8.4	299	4.7	1346.6	45.4
AR-2-3	32	18	<1	1.1	0.3	51.2	32.5	50.1	2.3	7	13.6	3.4	36.8	8.1	371	4.6	1258.3	41.6
ST-1	1231	6	<1	1.5	<0.1	45.5	18.3	13.3	1.5	2	2381.3	0.9	28.9	2.6	180	1.1	706.4	33.7

Table 6. Volatile trace element compositions (ppm) measured using aqua regia digestion.

Sample	Mo	Cu	Pb	Zn	Ni	As	Cd	Sb	Bi	Ag	Au	Hg	Tl	Se
AR-1	5.8	5.1	9	2	1.2	0.7	<0.1	0.5	1	<0.1	<0.5	<0.01	<0.1	<0.5
AR-2	12.8	4.5	10.8	18	1.8	1.4	<0.1	1.1	1.1	<0.1	1.1	0.01	<0.1	<0.5
AR-6	0.2	2.6	6.4	<1	2.3	<0.5	<0.1	0.1	1.9	<0.1	2.5	<0.01	<0.1	<0.5
AR-7	<0.1	2.7	9.4	<1	1.9	<0.5	<0.1	<0.1	1.1	<0.1	3	<0.01	<0.1	<0.5
AR-8	0.2	5.9	15.5	3	15.5	40.5	<0.1	1.4	0.6	<0.1	<0.5	0.05	<0.1	1.2
AR-11	0.8	2.7	17	4	3	4.1	<0.1	0.6	1.1	<0.1	<0.5	0.01	<0.1	0.9
AR-12	1.4	3.7	17.7	2	4.1	15.6	<0.1	0.7	1	<0.1	0.9	<0.01	<0.1	1.1
CAR-9	<0.1	2.2	10.2	<1	1.1	<0.5	<0.1	0.1	0.7	<0.1	0.9	<0.01	<0.1	<0.5
CAR-10	0.4	5.4	16.1	<1	1.9	<0.5	<0.1	0.5	1.5	<0.1	1	<0.01	<0.1	<0.5
CAR-11	0.5	4.7	22.4	1	1.5	2.3	<0.1	0.6	1.5	<0.1	1	<0.01	<0.1	1
AR-D2	1	4.2	15.5	3	2.6	7.7	<0.1	0.9	0.6	<0.1	1.2	<0.01	<0.1	<0.5
AR-D3	1.6	3.3	22.1	2	3.4	8.2	<0.1	0.9	1.3	<0.1	0.7	<0.01	<0.1	<0.5
AR-2-1	1.3	2	5.4	<1	1	<0.5	<0.1	0.3	0.6	<0.1	1	0.02	<0.1	<0.5
AR-2-3	7.7	2.2	12.7	1	2.2	1.8	<0.1	1	1.3	<0.1	<0.5	<0.01	<0.1	<0.5
ST-1	1	6.1	5.9	4	28.2	4.7	<0.1	<0.1	0.6	<0.1	<0.5	<0.01	<0.1	<0.5

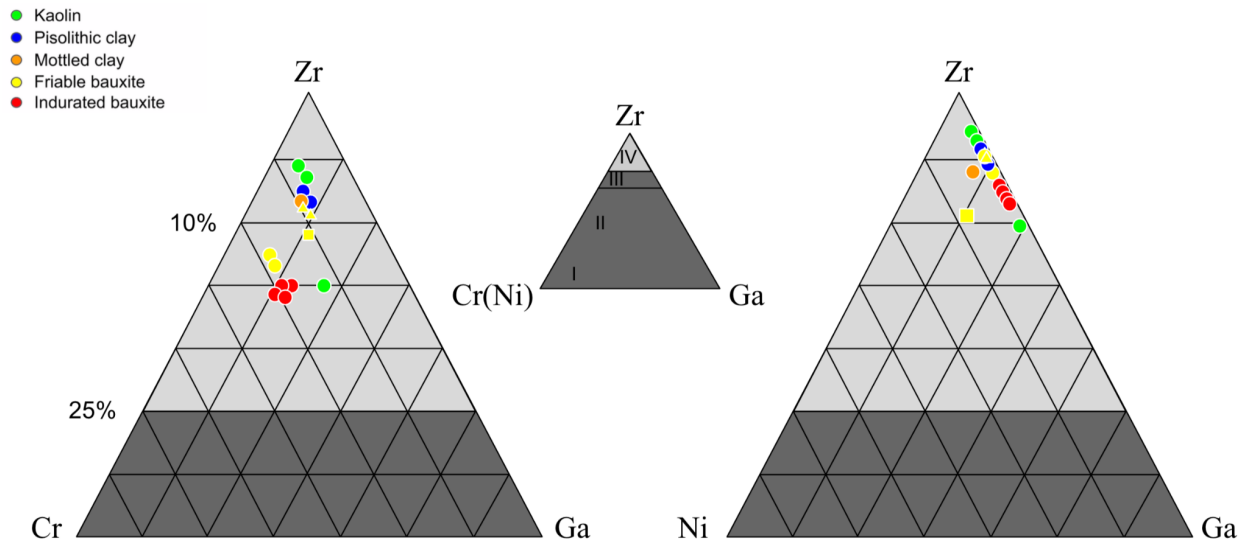

Figure 23. A ternary diagram with accompanying color code (top left) of the Zr-Cr(Ni)-Ga system that will indicate bauxite parent rock (Balasubramaniam et al., 1987). Circles denote samples from the main Arrow Road outcrop, triangles denote those from the second outcrop at the Arrow Road location, and the square represents sample ST-1.

Rare Earth Element Geochemistry

Rare Earth Elemental compositions for 15 bauxite and associated clay samples are shown in Table 7 and Table 8. Within the Arrow Road section, the sums of REEs, LREE, and HREEs range from 31.27 ppm to 170.03 ppm, 19.6 ppm to 83.94 ppm, and 18.4 to 86.09 ppm, respectively. The sample from Sturgis, MS had sums of REEs, LREEs, and HREEs of 45.44, 18.56, and 26.88, respectively.

At Arrow Road, REE, LREE, and HREE abundances decrease upsection from 77.94 to 45.44 ppm, 27.43 to 18.56, and 50.51 to 26.88, respectively (Fig. 24). A sharp increase at the stratigraphic position of 3.1 m (AR-8) is present. The La to Y ratio, which is used to determine the relative soil solution pH, remains relatively constant and below 1.0 throughout the Arrow Road section, however it increases from 0.17 to 0.55 between the stratigraphic positions 2.2 m and 3.1 m (Fig. 25). This ratio then drastically decreases to 0.21 at 3.2 m.

Generally, all samples collected from Arrow Road displayed similar REE trends when normalized to chondrite. At Arrow Road, chondrite-normalized REE trends gradually decreased until reaching Sm, which is then followed by a downward-pointing Eu anomaly. Trends then gradually increased from Gd to Lu. Sample ST-1 has a chondrite-normalized REE trend that decreases from La to Ce, increases from Ce to Nd, and decreases from Nd to Sm. This is followed by a downward-pointing Eu anomaly and then a decreasing trend between Gd and Lu. Tb has strong positive correlations with both Al_2O_3 and TiO_2.

Table 7. LREE compositions (ppm) measured using ICP-MS.

Sample	La	Ce	Pr	Nd	Sm	Sum LREE	Sum REE
AR-1	6.6	11.4	1.24	4.4	1.06	27.43	77.94
AR-2	9.6	19.1	2.08	7.3	1.95	44.4	110.31
AR-6	9.3	16.5	1.74	6.3	1.25	37.32	106.66
AR-7	16.2	36	4.22	15.4	3.03	78.66	117.13
AR-8	4.3	7.7	0.91	3.9	0.94	19.6	58.3
AR-11	4.5	9.1	0.94	3.7	1.08	22.21	59.3
AR-12	4.1	8.1	0.88	3.2	0.71	18.56	45.44
CAR-9	20.9	37.1	3.95	13.8	2.86	83.94	170.03
CAR-10	7.3	13.1	1.42	5	1.24	30.59	74.18
CAR-11	5.4	9.6	1.07	3.9	0.95	23.15	62.43
AR-D2	2.8	5.8	0.63	2.2	0.47	12.87	31.27
AR-D3	4	8.8	0.93	3.8	0.94	20.76	64.15
AR-2-1	7.1	13.2	1.3	4.6	1.24	30.89	98.14
AR-2-3	4.8	9.8	0.99	3.9	1.18	23.83	85.38
ST-1	12.9	24.1	4.38	22.7	5.04	76.71	127.15

Table 8. HREE compositions (ppm) measured using ICP-MS.

Sample	Eu	Gd	Tb	Dy	Ho	Er	Tm	Yb	Lu	Sum HREE	Sum REE
AR-1	0.34	2.39	0.63	4.94	1.18	4.12	0.63	4.39	0.72	50.51	77.94
AR-2	0.56	3.81	1	7.72	2	6.59	1.06	7.3	0.84	65.91	110.31
AR-6	0.35	1.88	0.48	3.64	0.84	2.85	0.47	3.26	1.2	69.34	106.66
AR-7	0.67	3.14	0.67	4.79	1.04	3.54	0.53	3.76	0.54	38.47	117.13
AR-8	0.26	1.59	0.38	2.74	0.66	2.2	0.34	2.41	0.57	38.7	58.3
AR-11	0.31	2.58	0.7	5.53	1.36	4.43	0.73	5.12	0.42	37.09	59.3
AR-12	0.2	1.37	0.35	2.8	0.66	2.16	0.34	2.29	0.38	26.88	45.44
CAR-9	0.73	4.6	1.14	8.7	2.05	6.82	1.07	7.38	1.23	86.09	170.03
CAR-10	0.36	2.17	0.59	4.55	1.08	3.46	0.56	3.92	0.63	43.59	74.18
CAR-11	0.29	1.94	0.5	3.92	0.95	3.11	0.52	3.52	0.56	39.28	62.43
AR-D2	0.14	0.83	0.23	1.73	0.39	1.37	0.23	1.58	0.27	18.4	31.27
AR-D3	0.27	2.02	0.54	4.42	1.02	3.51	0.52	3.8	0.58	43.39	64.15
AR-2-1	0.4	3.05	0.81	6.67	1.62	5.15	0.87	5.76	0.97	67.25	98.14
AR-2-3	0.34	2.82	0.74	5.87	1.43	4.95	0.79	5.28	0.89	61.55	85.38
ST-1	1.15	6.44	1.08	6.48	1.33	3.66	0.51	3.2	0.48	50.44	127.15

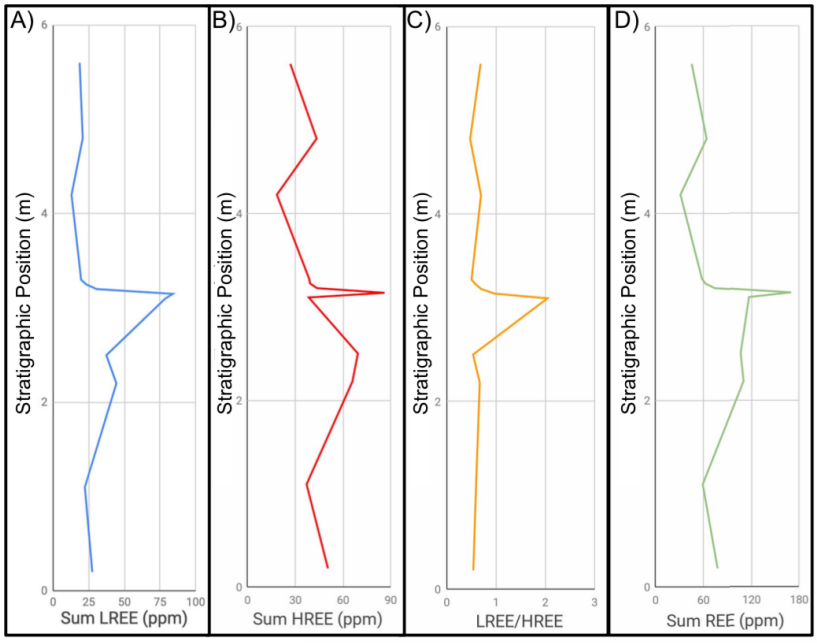

Fig. 23. The sums of LREEs, HREEs, and REEs as a function of stratigraphic position at the Arrow Road location.

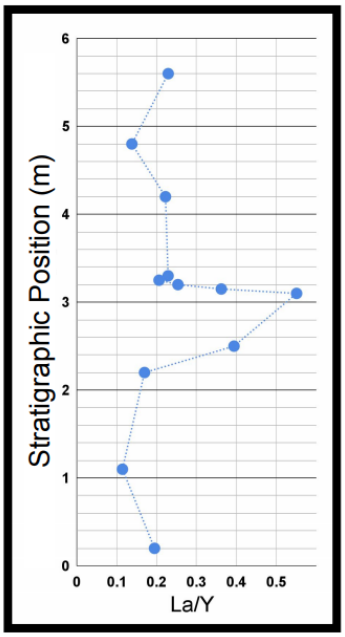

Figure 25. La/Y as a function of stratigraphic position at the Arrow Road location.

Isotope Geochemistry

At Arrow Road, $\delta^{18}O$ ranged from 6.1 to 17.8‰, while δD ranged between -98‰ to -57‰ (Table 9). Both $\delta^{18}O$ and δD decreased upsection (Fig. 26). The ratio of δD to $\delta^{18}O$ ranged from -0.33 to -0.06 and increased upsection. A significant decrease in $\delta^{18}O$ and δD was observed between the lower clayey zone and the upper bauxitic zone. Sample ST-1 had $\delta^{18}O$ and δD values of 16.4 and -58‰.

All samples with the exception of AR-D2 plot to the right of the boehmite equilibrium line in a bivariate plot of $\delta^{18}O$ and δD (Fig. 27). All indurated bauxites plotted to the left of the Supergene/Hypogene (S/H) line in a bivariate diagram of $\delta^{18}O$ and δD, suggesting a supergene origin. The remaining samples plotted to the right of this line, suggesting a hypogene origin (Fig. 28). Paleotemperature of the basal kaolin at Arrow Road was found to be ~34°C to 36°C, while the basal pisolithic clay was 30°C to 31°C (Fig. 29).

Table 9. Bulk isotope values obtained using IR-MS and an elemental analyzer.

Sample	$\delta^{18}O$ ‰	δD ‰	$\delta^{13}C$ ‰
AR-1	16.9	-57	-9.2
AR-2	16.9	-67	-4.9
AR-6	17.8	-54	-19.9
AR-7	17.5	-64	-27.3
AR-8	12.8	-72	-7.9
AR-11	14.3	-63	-12.4
AR-12	12.2	-79	-12.7
CAR-10	17.1	-64	-18.8
CAR-11	16.1	-63	-20.3
AR-D2	6.1	-98	-7.4
AR-D3	10.9	-91	-14.6
ST-1	16.4	-58	-19.2

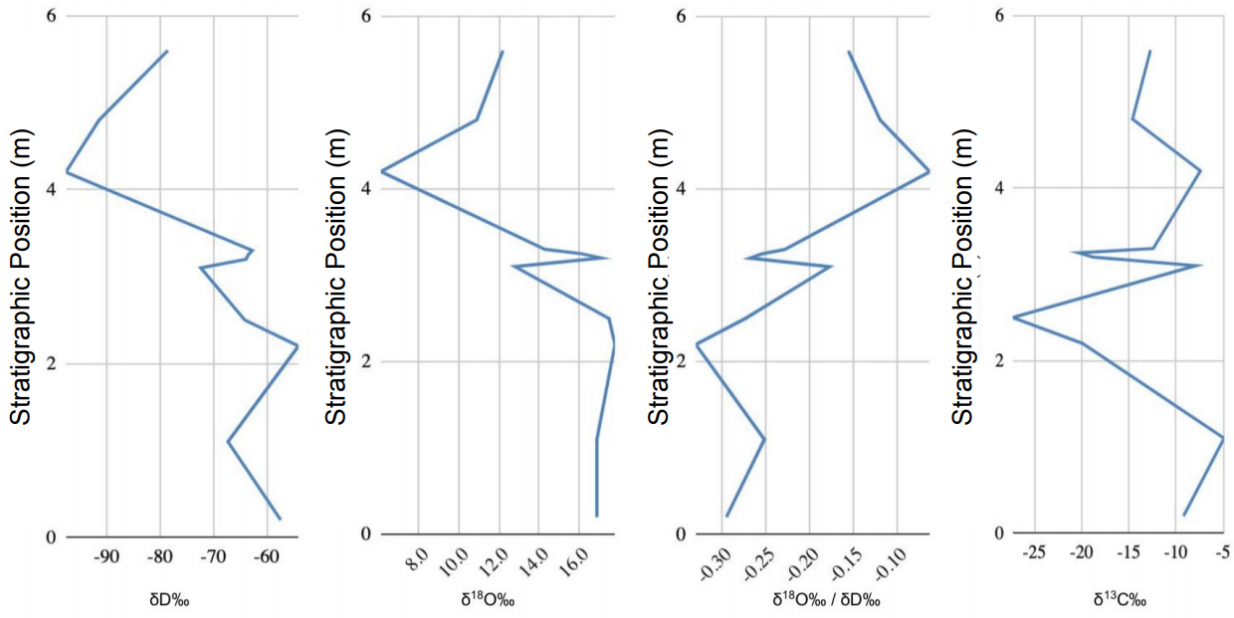

Figure 26. δD ‰, $\delta^{18}O$ ‰, δD ‰/$\delta^{18}O$ ‰, and $\delta^{13}C$ ‰ as a function of stratigraphic position at the main Arrow Road outcrop.

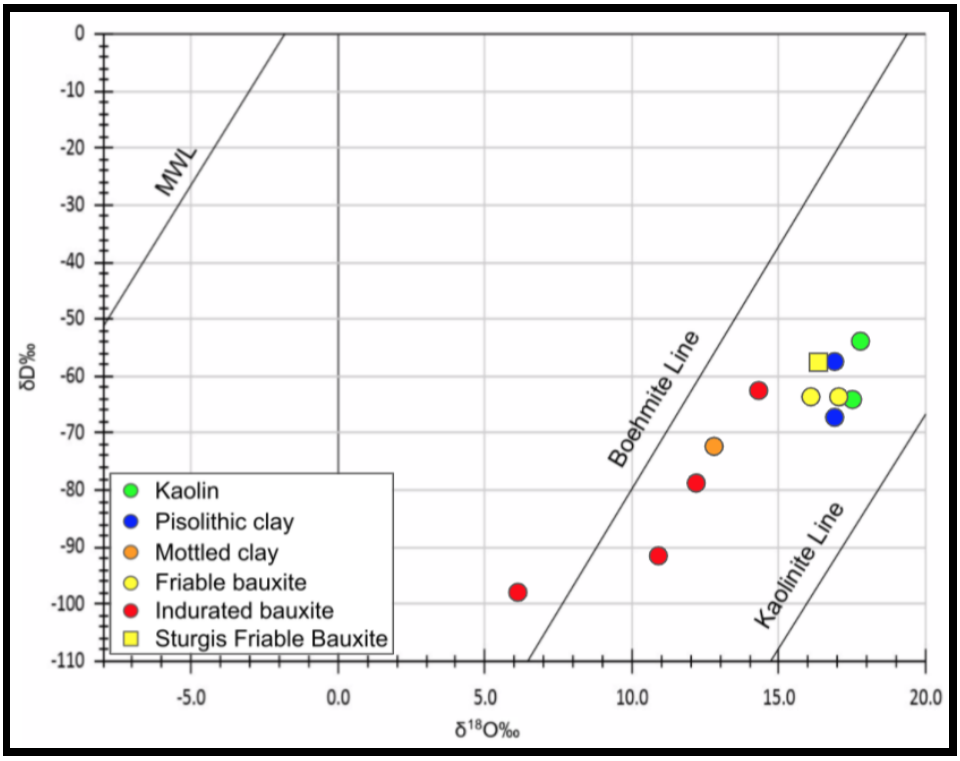

Figure 27. A bivariate diagram of δD and δ ^{18}O compositions showing the location of bauxite and clay samples in relation to the boehmite and kaolinite equilibrium lines.

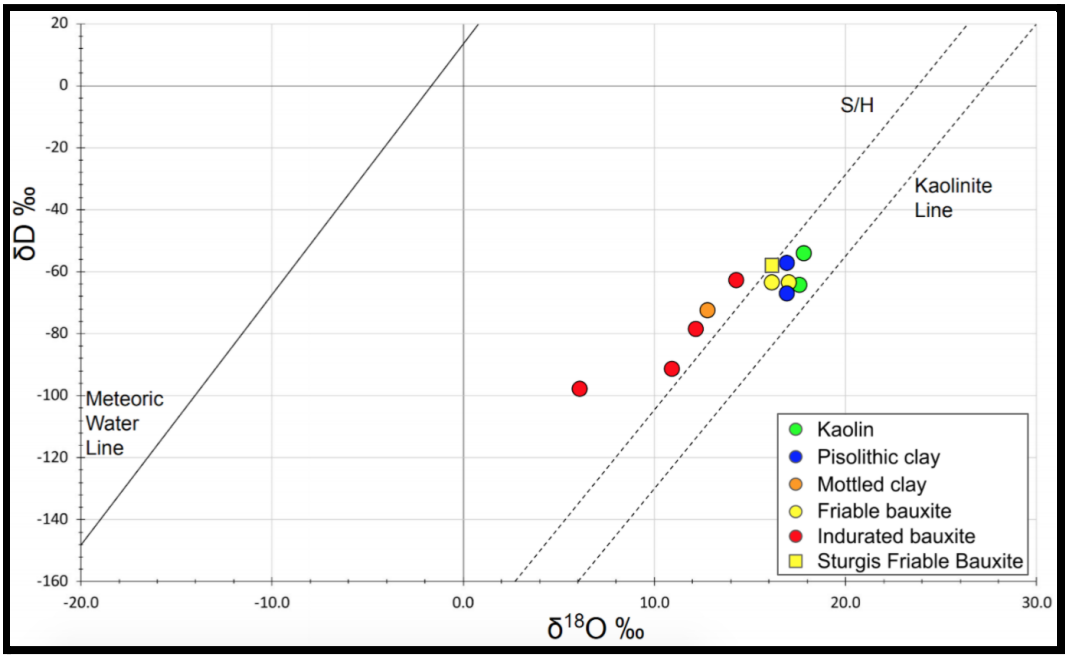

Figure 28. A bivariate diagram of δD and δ ^{18}O compositions showing the location of bauxite and clay samples in relation to a Supergene/Hypogene (S/H) line and kaolinite line, following Elahi et al. (2016).

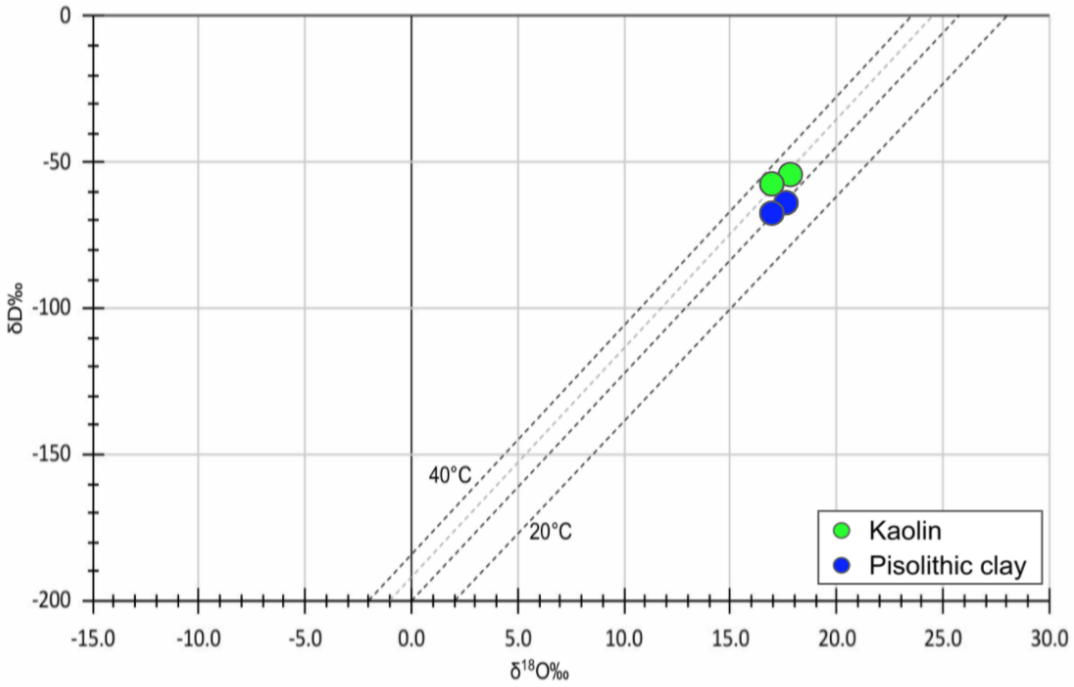

Figure 29. A bivariate plot of δD and $\delta^{18}O$ with kaolinite isotherm line denoting temperature at which the mineral crystallizes, following Feng and Yapp, 2009.

$\delta^{13}C$ ranged from -4.9 to -27.3‰ at the main Arrow Road outcrop and remained relatively constant throughout the section. The lowest value was observed within the interpreted plasmic zone, while the highest was in the interpreted saprolite immediately above. Sample ST-1 had a $\delta^{13}C$ value of -19.2‰.

Loss-on-Ignition

At Arrow Road, total LOI (LOI_{total}) ranged from 12.50% to 24.47% and did not vary substantially going upsection (Table 10; Fig. 30). The highest and lowest LOI_{total} percentages belonged to samples AR-7 and AR-8, respectively, which were both located near the vertical center of the outcrop. LOI_{total} increased from 18.03% to 19.05% between samples CAR-10 and CAR-11, while also increasing from 17.30% to 21.70% between samples AR-2-1 and AR-2-3. Sample ST-1 had the lowest LOI_{total} of any samples analyzed at 11.78%.

LOI after being heated to 550°C (LOI_{550}) ranged from 10.85% to 21.59% at the main Arrow Road outcrop. It closely followed the trend observed in LOI_{total} and the highest and lowest LOI_{550} also belonged to samples AR-7 and AR-8, respectively. LOI_{550} increased from 16.07% to 16.27% between samples CAR-10 and CAR-11 and from 15.48% to 18.57% between samples AR-2-1 and AR-2-3. Sample ST-1 also had the lowest LOI_{550} at 9.47%.

LOI after being heated to 950°C (LOI_{950}) ranged from 1.65% to 3.51% at the main Arrow Road outcrop and generally increased upsection. LOI_{950} increased from 1.97% to 2.78% between samples CAR-10 and CAR-11 and from 1.83% to 3.13% between samples AR-2-1 and AR-2-3. Sample ST-1 also had an LOI_{950} of 1.55%.

At Arrow Road, LOI values were used to predict Al_2O_3 content in gibbsitic bauxite samples based on the relationship proposed by Zhang et al. (2018):

$$Al_2O_3 \text{ Content} = 10.55e^{0.056(LOI)} \quad \text{Eq. 4}$$

The values obtained from this equation showed a moderate correlation ($r^2 = 0.504$; n = 6) with values obtained through the use of ICP-OES. LOI_{550} was found to have a stronger correlation with Al_2O_3 ($r^2 = 0.737$; n =6).

Organic carbon (OC) and inorganic carbon (IC) contents were calculated using the equations discussed in Dean (1974, 1999):

$$OC = (LOI_{550})*0.5 \quad \text{Eq. 5}$$

$$IC = (LOI_{950})*0.273 \quad \text{Eq. 6}$$

Table 10. Loss-on-ignition values for each sample.

Sample	LOI_{105} (%)	LOI_{550} (%)	LOI_{950} (%)	LOI_{totoal} (%)
AR-1	1.50	13.15	1.66	14.81
AR-2	0.93	15.80	2.50	18.30
AR-6	1.03	16.66	1.81	18.47
AR-7	3.30	21.59	2.88	24.47
AR-8	1.14	10.85	1.65	12.50
AR-11	1.12	15.72	2.86	18.58
AR-12	2.00	14.85	1.94	16.79
CAR-9	0.42	11.42	2.03	13.46
CAR-10	0.27	16.07	1.97	18.03
CAR-11	0.54	16.27	2.78	19.05
AR-D2	1.98	12.65	2.53	15.17
AR-D3	1.70	17.91	3.51	21.43
AR-2-1	5.49	15.48	1.83	17.30
AR-2-3	1.82	18.57	3.13	21.70
ST-1	1.55	9.47	2.31	11.78

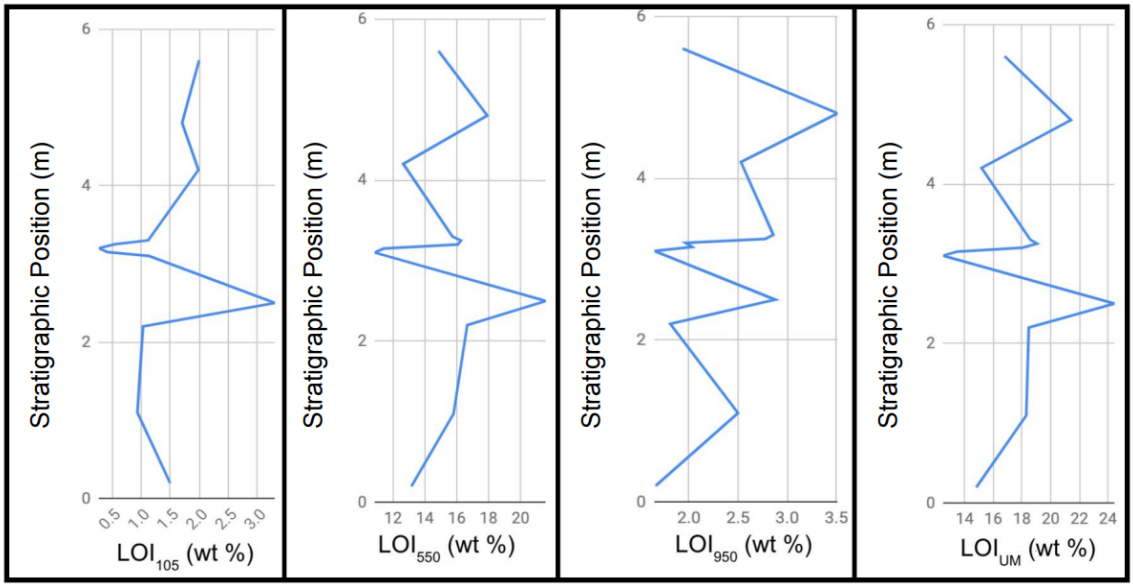

Figure 30. Percent LOI (105, 550, 950, and total) as a function of stratigraphic position at the main Arrow Road outcrop.

OC and IC were summed to approximate total carbon. There was a weak correlation with total C in bauxite samples ($r^2 = 0.107$, n = 6), but a strong correlation with total C values in the clays present at Arrow Road ($r^2 = 0.753$, n = 6). Among Arrow Road bauxite samples, LOI_{105} had the strongest correlation with total C ($r^2 = 0.893$, n = 6). Similarly, LOI_{105} had the strongest correlation with total C ($r^2 = 0.842$, n = 6) in clay samples.

LOI_{total} and LOI_{550} in gibbsitic bauxite were found to have strong correlations with Ga ($r^2 = 0.855$, n = 6; $r^2 = 0.848$, n = 6). Weak to moderate correlations were found between LOI_{105} and Ga as well as LOI_{950} ($r^2 = 0.009$, n = 6; $r^2 = 0.338$, n = 6).

LOI_{550} had a moderate negative correlation with $\delta^{13}C$ ($r^2 = 0.621$, n = 12). There was no correlation observed between LOI_{105} and LOI_{950} and $\delta^{13}C$ ($r^2 = 0.058$, n = 12; $r^2 = 0.06$, n = 12).

4. DISCUSSION

Genetic Classification

The 5 distinct lithologic zones present in the Arrow Road section resemble horizons present in a typical lateritic profile. I interpret the three larger lithofacies that divide the section as the parent material, the lower clay-rich zone, and upper bauxitic zone. The lower clay-rich zone can be divided into three distinct sub facies. I interpret the pisolithic clay at the base as the saprolith, the kaolin as part of the plasmic zone, and the mottled clay as the mottled zone. The upper bauxitic zone lithofacies can be divided into two observable sub facies, a friable fragmental unit represented by the friable bauxite, and a lateritic duricrust represented by the indurated bauxite. This supports a lateritic origin for the Arrow Road bauxite, whether it be primary or secondary, as lateritization typically results in the separation of distinct horizons (Mondillo, 2020). Secondary lateritizations would result in a karst bauxite classification under the 2-fold system and a sedimentary classification under the 3-fold.

The Arrow Road bauxite plots in the high-Fe lateritic bauxite field in a binary diagram of Ni and Cr compositions, perhaps due to the underlying material being somewhat rich in Fe due to the presence of siderite nodules (Fig. 23). Major oxide data of the Arrow Road section followed trends typically associated with lateritic profiles. Percent available Al_2O_3 increased starting from the base of the plasmic zone, peaked in the mottled zone, and then decreased until the top of the lateritic gravel horizon. Percent available Fe_2O_3 followed a similar trend, increasing until it peaked near the contact of the duricrust and lateritic gravel horizons. Percent reactive SiO_2 decreased sharply starting at the base of the plasmic zone, stabilized slightly (still

decreasing) near the base of the mottled zone, and then decreased throughout the upper bauxitic zone.

The Sturgis deposit was previously mapped as lower Wilcox Group and was described as being a reworked bauxite (Pandya, 1973). This hypothesis is supported by an abundance of quartz sand in the matrix and crossbedding reported by Pandya (1973). Additionally, the variation between the Arrow Road orebody and the Sturgis bauxite suggests a difference in genetic histories (Fig. 31).

There was a strong positive correlation between TiO_2 and Al_2O_3 ($r^2 = 0.837$; n = 6), which suggests they are more concentrated in horizons that have experienced strong weathering.

Degree of Lateritization

As expected, the degree of lateritization increased upsection at Arrow Road. This is consistent with the typical lateritic profile in which silica decreases in proportion to Al_2O_3 and Fe oxide. This occurs as a result of chemical weathering of an *in situ* protolith and the subsequent removal of mobile elements (MacLean et al., 1997).

I interpret the decrease in REE abundance upsection at Arrow Road as a result of lateritization and horizonation. The sharp increase in REE abundance occurring near the boundary of the interpreted mottled zone and bauxitic zone could be due to a change in the dominating process at that point in bauxitization and the formation of distinct eluvial and illuvial horizons.

Dismantlement Pathway

The sample highest in REEs (CAR-9) plots in the "preservation of kaolinite field," while overlying samples plot forming in a linear pattern in the direction of the "dehydration" field ending two meters above with sample AR-D2 (Fig. 20). The last two samples in the section

(AR-D3 and AR-12) move in a retrograde fashion suggesting a change in the processes dominating bauxitization (Fig. 20). AAR-11 and AR-11 are also the only two bauxite samples found to contain boehmite (Appendix 2). Additionally, AR-D2 is the only sample that plots to the left of the boehmite equilibrium line in a binary diagram of $\delta^{18}O$ and δD (Fig. 27), indicating that low-temperature diagenesis may have occurred. Indeed, the pisoliths also vary in composition between samples AR-11 and AR-D2, which have an internal matrix composed of Al and CAR-14, which are mostly Si. The strong positive correlations between TiO_2 and high field strength elements within bauxite samples suggests that they share similar geochemical behaviors and remain stable throughout bauxitization, which may reflect the overall trend towards dehydration observed between the lower FFU and lower duricrust (Liu et al., 2010; Zarasvandi et al., 2012).

Protolith

The interpreted protolith for the Arrow Road bauxite is the pisolithic clay at the base of the profile. $\delta^{13}C$ was depleted at this location relative to the rest of the profile, suggesting subaerial exposure and isotope exchange (Hajikazemi et al., 2010). Additionally, normalized REE values of pisolithic clay closely resemble those of the bauxite located upsection. Chondrite-normalized REE values deviate from those observed from the Sturgis bauxite, suggesting either a different origin or protolith (Fig. 31). This is consistent with the Sturgis bauxite being mapped as reworked bauxite within the lower Wilcox Group.

Thompson (1981) rules out genesis by terra rosa, lateritization of igneous materials, and/or a saprolite complex due to association with units that bauxite is not usually associated with (fluvial deltaic muds, and sands, as well as tidal flat and prodelta muds). Given this conclusion, it was expected that the data would plot between or near the sandstone, shale/slate,

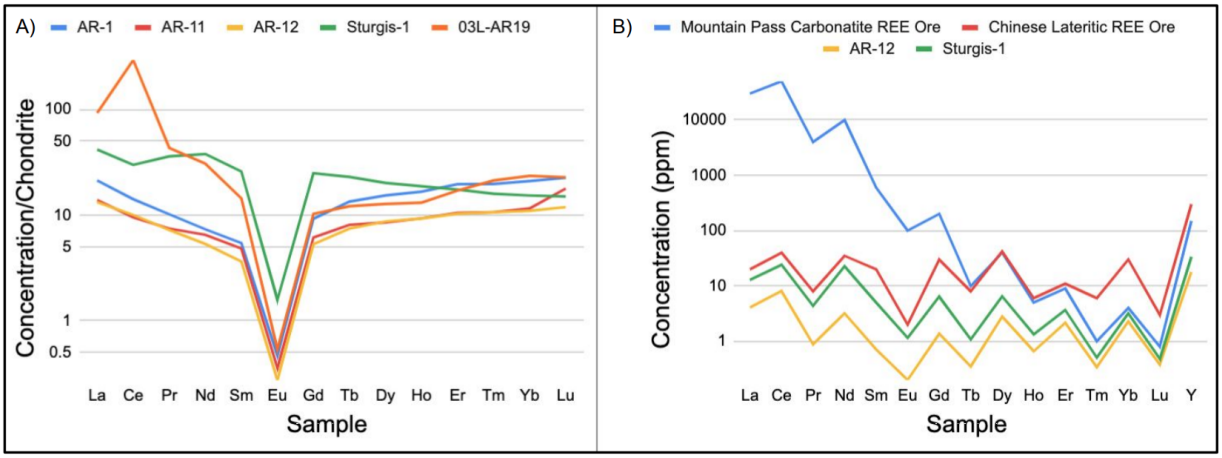

Figure 31. A: Chondrite-normalized REE trends associated with three bauxites from the Arrow Road location juxtaposed beside the REE trend associated with the sample collected from the Sturgis deposit and one bauxite sample from the Pulaski-Saline deposit. B: REE concentrations from an Arrow Road bauxite as well as sample ST-1 juxtaposed beside REE concentrations from two of the world's premier sources of REEs (i.e., Mountain Pass and Chinese Laterite). Additional data sourced from Van Gosen and Choat (2019) and Haxel et al. (2002).

and carbonate points (Fig. 23). Instead, the data plotted within the "high-iron lateritic bauxite" field and in close proximity to the sandstone and granite points. It should be noted however that there is no point within the bivariate diagram of Ni and Cr reflecting a bauxitic protolith, which would be necessary in order to determine if the bauxite was the product of secondary lateritization. Additionally, the Sturgis bauxite plotted in close proximity to the sandstone reference point within the high iron lateritic bauxite field despite being reworked and thus, by definition, a karst bauxite. It is therefore suggested that this diagram be reevaluated to take into account sedimentary bauxites that do not overly carbonate bedrock.

Secondary lateritization of the pisolithic clay would imply that the pisolithic clay formed due to lateritization of its underlying parent material. Stratigraphically, this would imply successive periods of subaerial exposure, followed by erosion, and return to subaerial exposure characteristic of a coastal setting.

Previous investigations show that neither upland nor underlying strata are igneous in origin (Thompson, 1981). Instead, upland and underlying strata are dominated by shales,

sandstones, and carbonates. The La to Y ratio of the interpreted protolith pisolithic clays is below 1 (Fig. 25), which suggests that an acidic paleoenvironment was present at the time and supports the conclusions made from the ternary diagram (Maksimovic and Panton, 1991; Ellahi et al., 2016). The strong positive correlation between Tb and Al_2O_3 may be associated with the formation of heavy minerals (e.g. anatase, rutile, and titanite) (Karadag et al., 2009). It should be noted however that none of these were identified during XRD analyses discussed herein or during the most recent study (Thompson, 1981)

Paleoenvironment

Thompson (1981) argued that the unique structure of the north Mississippi bauxites could be due to pH fluctuations associated with facies changes between fluvial and paludal settings. Additionally, pH fluctuations created conditions allowing for the selective precipitation and differential flocculation of high Al clays and Fe (Thompson, 1981). If this were true, the La to Y ratio would fluctuate as a function of pH. La/Y > 1 is indicative of basic soil solution pH, while La/Y <1 is indicative of acidic conditions (Ellahi et al., 2016). The ratios of La to Y remain below 1 throughout the Arrow Road section, suggesting that an acidic soil solution was present throughout bauxitization, although a sharp increase in this ratio from 0.17 to 0.55 occurs at the transition from the interpreted plasmic zone to the mottled zone (Fig. 25). This is believed to be due to the differentiation of an eluvial and illuvial horizon as the ratio of LREEs to HREEs follows a very similar trend. The strong positive correlation between SiO_2 and Al_2O_3 as well as a strong negative correlation between Al_2O_3 and Fe_2O_3 suggests that the majority of Al_2O_3 is contained within aluminosilicate minerals as opposed to gibbsite or boehmite, which supports the hypothesis of an acidic paleoenvironment.

The sum of REEs (ΣREE) decreases upsection, supporting the hypothesis of an acidic paleoenvironment; REEs are more easily removed from the weathering profile under these conditions (Nesbitt, 1979; Karadag et al., 2009). In addition, Thompson (1981) documented lignitic bauxite at Arrow Road and proposed the possibility of a paludal environment dominated by reed-like plants, which would likely have been acidic. This hypothesis of a lowland swamp- to bog-like environment is supported by the rhizoliths and geochemical data presented herein.

Concentrations of $\delta^{13}C$ vary throughout the Arrow Road section, suggesting a complex history in regards to photosynthetic uptake of CO_2. Organic matter produced from atmospheric CO_2 through C_4 and C_3 photosynthesis typically have $\delta^{13}C$ values near -14‰ and -27‰, respectively (O'Larry, 1988; Kanduc et al., 2005). Among bauxite at Arrow Road, only sample AR-7 (lower clayey zone) was characterized by a $\delta^{13}C$ value (-27.3‰) consistent with that of organic matter produced by C_3 plants (Fig. 26). Since C_4 photosynthesis likely evolved between 30 and 20 Ma (Sage, 2004), the highly negative $\delta^{13}C$ values must be the result of other processes.

Diagenetic History

Sample AR-D2 marks the only point within the upper bauxitic zone where $\delta^{13}C$ is similar to that of atmospheric CO_2. Additionally, it is the only sample where H and O isotope values lie to the left of the boehmite equilibrium line. Boehmite was only detectable in sample AR-D2 and AR-11, but neither of the two above these, which suggest that this sample was subjected to some form of diagenetic alteration after deposition. Due to the absence of any erosional surface, it is not believed that subaerial exposure occurred, but that some isotope exchange occurred at a shallow depth. Pisolith composition also varies between AR-D2 and CAR-14, while the matrix remains the same, indicating that the pisolith matrices in samples AR-11 and AR-D2 are boehmite as opposed to gibbsite.

The Liesegang banding residing between samples CAR-10 and CAR-11 as well as between CAR-2-1 and CAR-2-3 also marks a distinct geochemical and mineralogic boundary. Due to the highly undulatory geometry of the banding, it is believed to be a result of fingered or preferential flow of groundwater at the time of alteration. The Liesegang banding present within sample CAR-14 crosscuts a rhizolith, which itself crosscuts a pisolith, which indicates that the chronological series of events from first to last were as follows: (1) pisolith formation, (2) root formation and mineralization, and (3) fracturing followed by precipitation of Liesegang banding. In addition, the chemical indices V and STI suggest the chemical weathering subjected to the material increased upsection.

Economic Value

Only samples CAR-10, AR-2-1, and AR-2-3 contain Al_2O_3 in a concentration greater than 40 %, the common cut-off grade (Fig. 32). Additionally, only sample AR-D2 contains Sc in concentrations greater than 0.002%, the ore cutoff grade estimate sufficient for extraction from red mud following the removal of Al (Fig. 32). None of the Arrow Road bauxites contained an REE concentration significant enough to warrant mining for REEs. Sample ST-1 contained a significantly larger concentration of REEs perhaps as a result of its reworked genesis. Historically notable REE orebodies such as the Mountain Pass carbonatite and a Chinese lateritic deposit (see Haxel et al., 2002) as well as bauxite from the Pulaski-Saline district, which are not considered to be a valuable source of REEs, each contained REEs in concentrations greater than those discussed herein (Fig. 31). 90 percent of the world's Ga is reported to come from bauxite residue, from which the ore had a concentration between 30 and 90 ppm (Rosi, 1980). All of the bauxite samples analyzed herein contain a Ga concentration within that range (Fig. 31). Thus, neither Arrow Road, nor Sturgis appear to be viable primary sources of Ga, however the

byproduct of their refinement could be a secondary source. As noted by Thompson (1981), the orebodies in North Mississippi are not extensive enough to warrant extraction, and the results of this research have demonstrated that the most well-exposed location lacks significant enough concentrations to warrant extraction. Because this research only serves as a pilot study in terms of exploring economic potential, further research would be needed to generalize the entirety of the North Mississippi bauxite regions in terms of REE composition. In particular, my recommendation is that geochemical data should be collected in the vicinity of Big Hill and Smoky Top due to their historical mining activity if an exploratory study were to commence.

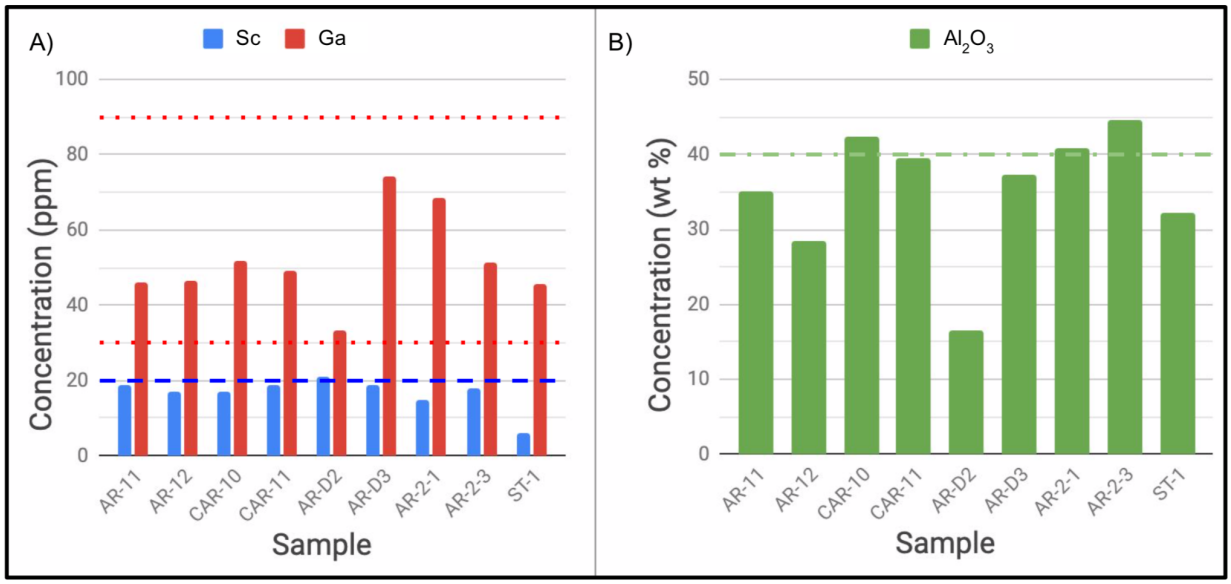

Figure 32. A: Bar graph showing the concentrations of Sc and Ga from bauxite samples studied herein. Blue Dashed Line = 20 ppm Sc cutoff grade; Red Dotted Line = Ga 30-90 ppm cutoff range. B: Al concentration of bauxites analyzed as part of this study with the Al ore cutoff grade (40 %) denoted by the green alternating dashed/dotted line.

Loss-on-Ignition

The correlation between LOI_{550} and Al_2O_3 could be due to the evaporation of water contained within the crystal lattice of some minerals, mainly kaolinite. Alternatively, a relationship between LOI_{550} and the dehydroxylation of gibbsite could be responsible for this correlation as this begins at a temperature of 220°C and is complete by 350°C (Kloprogge et al., 2002). I recommend that further studies be conducted to determine the relationship between temperature specific LOI Al_2O_3 content in gibbsitic bauxite as this would provide a quick and cost-effective solution during bauxite prospecting.

5. CONCLUSIONS

The findings of this research demonstrate that the bauxites located at Arrow Road in Pontotoc County, Mississippi were formed through *in situ* weathering of a sedimentary protolith under warm and acidic conditions. Pisolithic clay and kaolin near the base of the profile formed at paleotemperatures of 30 to 31°C and 34 to 36°C, respectively. Bauxites at the location have a geochemical suite that closely resembles that from the typical lateritic bauxite profile, yet they lack a significant enough concentration of Al_2O_3, Ga, or Sc to warrant any large-scale mining operations. The highest $\delta^{13}C$ value was observed in the portion of the section interpreted as the parent material, confirming that it had been exposed subaerially or shallow enough to allow for isotopic exchange. Fieldwork results in the form of horizonation and rhizoliths also support the occurrence of lateritization taking place; it remains unclear whether this was primary or secondary due to strata underlying the pisolithic clay being unexposed. SEM-EDS data confirmed that the Sturgis bauxite did not contain pisoliths with the same chemical composition as those in Pontotoc and thus, they likely are not the parent material that is being reworked. It is recommended that future work be conducted to determine the REE composition and extent of bauxite deposits in Mississippi in order to make a more complete interpretation of economic viability.

LIST OF REFERENCES

AKAYEMOV, S.T., PASTUKHOVA, M.V., TENYAKOV, V.A., and YASAMANOV, N.A., 1975, Time and Circumstances of Bauxite Formation from the Lateritic Crusts of the Earth's Equatorial Zone: Problems of Bauxite Genesis. Izvestiya Akademi Nauka, Moscow, p. 55–78

ALEVA, G.J.J., 1994, Laterites: Concepts, Geology, Morphology and Chemistry: International Soil Reference and Information Centre (ISRIC), Wageningen, 169 p.

AUTIN, W.J., BURNS, S.F., MILLER, B.J., SAUCIER, R.T., and SNEAD, J.I., 1991, Quaternary Geology of the Lower Mississippi Valley, *in* Morrison, R.B. (eds.), Quaternary Nonglacial Geology: Conterminous US Geological Society of America, Boulder, p. 547–582.

BÁRDOSSY, G.Y., 1982, Karst Bauxites: Bauxite Deposits on Carbonate Rocks: Elsevier Science Publishers, Amsterdam, 441 p.

BÁRDDOSSY, G.Y. and ALEVA, G.J.J., 1990, Developments in Economic Geology. Elsevier Scientific Publication, Amsterdam, 624 p.

BÁRDOSSY, G.Y., and COMBES, P.J., 1999, Karst Bauxites: Interfingering of Deposition and Palaeoweathering, *in* Thiry, M. and Simon-Coincon, R. (eds.), Palaeoweathering, Palaeosurfaces and Related Continental Deposits: Alden Press, p. 189–206.

BEAUVAIS, A., 1991, Paléoclimats et Dynamique d'un Paysage Cuirassé du Centrafrique. Morphologie, Pétrologie et Géochimie. Unpublished M.S. thesis, University Poitiers, 315 p.

BERTHIER, P., 1821, Analyse de L'alumine Hydratée des Baux: Annales Mines, v. 6, p. 531–534.

BINNEMANS, K., PONTIKES, Y., JONES, P.T., VAN GERVEN, T., and BLANPAIN, B., 2013, Recovery of Rare Earths from Industrial Waste Residues: A Concise Review: Third International Slag Valorisation Symposium Proceedings, p. 191–205.

BIRD, M.I. and CHIVAS, A.R., 1993, Geomorphic and Paleoclimatic Implications of an Oxygen-Isotope Chronology for Australian Deeply Weathered Profiles: Australian Journal of Earth Sciences, v. 40, p. 345–358.

BOGATYREV, B.A., ZHUKOV, V.V., and TSEKHOVSKY, Y.G., 2009, Formation Conditions and Regularities of Large and Superlarge Bauxite Deposits: Lithology and Mineral Resources, v. 44, p. 135–151.

BOULANGE, B., BOUZAT, G., and POULIQUEN, M., 1996, Mineralogical and Geochemical Characteristics of Two Bauxitic Profiles, Fria, Guinea Republic: Mineralium Deposita, v. 31, p. 432–438.

BUCHER, W., 1921, Logan's Explanation of the Origin of Indiana's "Kaolin": Society of Economic Geologists, v. 16, p. 481–492.

COMBES, P.J., 1990, Typologie, Cadre Géodynamique et Génèse des Bauxites Françaises: Geodinamica Acta, v. 4, p. 91–109.

CONANT, L.C., 1965, Bauxite and Kaolin Deposits of Mississippi Exclusive of the Tippah-Benton District: U.S. Geological Survey Bulletin. no. 1199-13, 66 p.

CUSHING, E.M., BOSWELL, E.H., and HOSMAN, R.L., 1964, General Geology of the Mississippi Embayment: U.S. Geological Survey Professional Papers, no. 448-B, 28 p.

DEAN, W.E., 1974, Determination of Carbonate and Organic Matter in Calcareous Sediments and Sedimentary Rocks by Loss on Ignition: Comparison with Other Methods: Journal of Sedimentary Petrology, v. 44, p. 242–248.

DEAN, W.E., 1999, The Carbon Cycle and Biogeochemical Dynamics in Lake Sediments: Journal of Paleoclimatology, v. 21, p. 375–393.

DOCKERY, D.T., 1996, Toward a Revision of the Generalized Stratigraphic Column of Mississippi: Mississippi Geology, v. 17, p. 1–9.

DUPPLANTIS, M.J., 1975, Depositional Systems in the Midway and Wilcox Groups, Mississippi: Unpublished M.S. thesis, University Mississippi, Oxford, 82 p.

EHRLICH, H.L., 2002, Geomicrobiology: Marcel Dekker, New York, 768 p.

ELLAHI, S.S., TAGHIPOUR, B., ZARASVANDI, A., BIRD, M., and SOMARIN, A., 2016, Mineralogy, Geochemistry and Stable Isotope Studies of the Dopolan Bauxite Deposit, Zagros Mountain, Iran: Minerals, v. 6, no. 1, 20 p.

FENG, W. and YAPP, C.J., 2009, $^{18}O/^{16}O$ and D/H Ratios of Pedogenic Kaolinite in a North American Cenomanian Laterite: Paleoclimatic Implications. Geochimica et Cosmochimica Acta, v. 7, p. 6249–6263.

FOLEY, N.K, JASKULA, B.W., KIMBALL, B.E., and SCHULTE, R.F., 2017, Gallium, *in* Schulz K.J., DeYoung J.H., Seal R.R., and Bradley D.C. (eds.), Critical Mineral Resources of the United States—Economic and Environmental Geology and Prospects for Future Supply. US Department of the Interior.

FOLEY, N.K., and JASKULA, B.W., 2013, Gallium—a Smarter Metal: U.S. Geological Survey Fact Sheet, U.S. Department of Interior.

FORTIER, S.M., NASSAR, N.T., LEDERER, G.W., BRAINARD, J., GAMBOGI, J., and MCCULLOUGH, E.A., 2018, Draft Critical Mineral List-Summary of Methodology and Background Information—U.S. Geological Survey Technical Input Document in Response to Secretarial Order No. 3359: U.S. Geological Survey Open-File Report 2018-1021, 15 p.

FREEMAN, M.J., and DONALDSON, M. J., 2004, Major Mineral Deposits of Southwestern Western Australia: a Field Guide: Australia Department of Industry and Resources. East Perth. 45 p.

FRENZEL, M., KETRIS, M.P., SEIFERT, T., and GUTZMER, J., 2016, On the Current and Future Availability of Gallium: Resources Policy, v. 47, p. 38–50.

FREYSSINET, P.H., BUTT, C.R.M., MORRIS, R.C., and PIANTONE, P., 2005, Ore-forming Processes Related to Lateritic Weathering: Economic Geology, v. 100, p. 681–722.

GALLOWAY, W.E., GANEY-CURRY, P.E., LI, X., and BUFFLER, R.T., 2000, Cenozoic Depositional History of the Gulf of Mexico Basin: The American Association of Petroleum Geologists Bulletin, v. 84, p. 1743–1774.

GALLOWAY, W.E., WHITEAKER, T.L., and GANEY-CURRY, P., 2011, History of Cenozoic North American Drainage Basin Evolution, Sediment Yield, and Accumulation in the Gulf of Mexico Basin: Geosphere, v. 7, p. 938–973.

GIBSON, C., and HAYES, T., 2011, Indium and Gallium Overview: Edison Investment Research, 10 p.

GORDON, M., TRACEY, J.I., and ELLIS, M.W., 1958, Geology of the Arkansas Bauxite Region: U.S. Geological Survey Professional Paper 299, 268 p.

HAJIKAZEMI, E., AL-AASM, I.S., CONIGLIO, M., 2010. Subaerial Exposure and Meteoric Diagenesis of the Cenomanian-Turonian Upper Sarvak Formation, Southwestern Iran: Geological Society of American Special Publication, v. 330,p. 253–272.

HAO, X., LEUNG, K., WANG, R., SUN, W., and LI, Y., 2010, Geomicrobiology of Bauxite Deposits: Geoscience Frontiers, v. 1, p. 81–89.

HAXEL, G., ORRIS, J.B., STAUFFER, P.H., and HENDLEY, J.W., 2002, Rare Earth Elements: Critical Resources for High Technology. United States Geological Survey Fact Sheet, 4 p.

HEIRI, O., LOTTER, A.F., and LEMCKE, G., 2001, Loss on Ignition as a Method for Estimating Organic and Carbonate Content in Sediments: Reproducibility and Comparability of Results: Journal of Paleolimnology, v. 25 p. 101–110.

HERRINGTON, R., MONDILLO, N., BONI M., THORNE, R., and TAVLAN, M., 2016, Bauxite and nickel-cobalt lateritic deposits of the Tethyan Belt. In: Richards J (ed.) Tectonics and Metallogeny of the Tethyan Orogenic Belt. Special Publication n. 19, 349–387. Littleton, CO: Society of Economic Geologists, Inc.

HOSMAN, R.L. and WEISS, J.S., 1991, Geohydrologic Units of the Mississippi Embayment and Texas Coastal Uplands Aquifer Systems, South-central United States: U.S. Geological Survey Professional Paper, no. 1416-B, 19 p.

JACKSON, M.L., 1979, Soil Chemical Analysis – Advanced Course, second ed. 11th Printing. Published by the author, Madison, WI.

KANDČ, T., MARKIC, M. and PEZDIČ, J., 2005, Stable Isotope Geochemistry of Different Lithotypes of the Velenje Lignite (Slovenia): Geologija, v. 48, p. 83-95.

KARADAĞ, M.M., KUPELI, S., ARYK, F., AYHAN, A., ZEDEF, V., and DOYEN, A., 2009, Rare Earth Element (REE) Geochemistry and Genetic Implications of the Mortas Bauxite Deposit (Seydisehir/Konya-Southern Turkey). Chemie der Erde Geochem, v. 69, p. 143–159.

LIU, X.F., WANG, Q.F., DENG, J., ZHANG, Q.Z., SUN, S., and MENG, J., 2010, Mineralogical and Geochemical Investigations of the Dajia Salento-Type Bauxite Deposits, Western Guangxi, China Journal of Geochemical Exploration, v. 105 p. 137–152.

MACLEAN, W.H., BONAVIA, F.F., SANNA, G., 1997, Argillite Debris Converted to Bauxite During Karst Weathering: Evidence from Immobile Element Geochemistry at the Olmedo Deposit, Sardinia: Mineralium Deposita, v. 32, p. 607–616.

MAC NEIL, 1951, Fern Spring Member of the Wilcox Formation in Mississippi: American Association of Petroleum Geology Bulletin, no. 35, p. 1062–1063.

MAKSIMOVIC, Z. and PANTO, G., 1991, Contribution to the Geochemistry of the Rare Earth Elements in the Karst-Bauxite Deposits of Yugoslavia and Greece: Geoderma, v. 51, p. 93–109.

MAMELI, P., MONGELLI, G., OGGIANO, G., and DINELLI, E., 2007, Geological, Geochemical and Mineralogical Features of Some Bauxite Deposits from Nurra (Western Sardinia, Italy): Insights on Conditions of Formation and Parental Affinity: International Journal of Earth Science, v. 96, p. 887–902.

MCCULLOUGH, E. and NASSAR, N.T., 2017, Assessment of Critical Minerals—Updated Application of an Early-Warning Screening Methodology: Mineral Economics, v. 30, p. 257–272.

MELLEN, F.F., 1939, Winston County Mineral Resources: Mississippi Geological Survey Bulletin, no. 38, 169 p.

MONDILLO, N., HERRINGTON, R., and BONI, M., 2020, Bauxites: Encyclopedia of Geology, 14 p.

MURRAY, G.E., 1961, Geology of the Atlantic and Gulf Coastal Province of North America: Harper and Brothers, New York, 692 p.

NATARAJAN, K.A., MODAK, J.M., and ANAND, P., 1997, Some Microbiological Aspects of Bauxite Mineralization and Beneficiation: Minerals and Metallurgical Processing, v. 14, p. 47–53.

NESBITT, H.W., 1979, Mobility and Fractionation of Rare Elements During Eeathering of a Granodiorite: Nature, v. 279, p. 206–210.

OCHSENKÜHN-PETROPULU, M., LYBEROPULU, T., and PARISSAKIS, G., 1994, Direct Determination of Lanthanides, Yttrium and Scandium in Bauxites and Red Mud from Alumina Production: Analytica Chimica Acta, v. 296, p. 305–313.

O'LARRY, M.H., 1988: Carbon Isotopes in Photosynthesis: Bioscience, v. 38, p. 328–336.

PANDYA, D.N., 1973, A Study of the Bauxite Deposits Along the Midway- Wilcox Contact in Okitibbeha County, Mississippi: Unpublished M.S. thesis, Mississippi State University, Starkville, 62 p.

PATTERSON, S.H., 1967, Bauxite Reserves and Potential Aluminum Resources of the World: U.S. Geological Survey Bulletin, no. 1228, 175 p.

PRICE, G.D., VALDES, P.J., and SELLWOOD, B.W., 1997, Prediction of Modern Bauxite Occurrence: Implications for Climate Reconstruction: Palaeogeography Palaeoclimatology Palaeoecology, v. 131, p. 1–13.

PRICE, J.R. and VELBEL, M.A., 2003, Chemical Weathering Indices Applied to Weathering Profiles Developed on Heterogeneous Felsic Metamorphic Parent Rocks: Chemical Geology, v. 202, p. 397–416.

REED, D.F., 1952, Investigation of High Aluminum Clays and Bauxite of Northeastern Mississippi: U.S. Bureau of Mines Reports, no. 4827, 84 p.

REID, S., TAM, J., YANG, M., and AZIMI, G., 2017, Technospheric Mining of Rare Earth Elements from Bauxite Residue (Red Mud): Process Optimization, Kinetic Investigation, and Microwave Pretreatment: Scientific Reports, v. 7, no.15252, 9 p.

SAGE, R.F., 2004, The Evolution of C_4 Photosynthesis: New Phytologist, v. 161, p. 341-370.

SCHELLMANN, W., 1986, Geochemical Differentiation in Laterite and Bauxite Formation: Catena, v. 21, p. 131–143.

SCHROLL, E. and SAUER, D., 1968, Beitrag zur Geochemie von Titan, Chromium, Nickel, Cobalt, Vanadium und Molybdan in Bauxitischen Gesteinen und das Problem der Stofflichen Herkunft des Aluminiums: Travaux du ICSOBA, v. 5, p. 83–96.

SHARMAN, G.R., COVAULT, J.A., STOCKLI, D.F., WROBLEWSKI, A.J., and BUSH, M.A., 2017, Early Cenozoic Drainage Reorganization of the United States Western Interior‐Gulf of Mexico Sediment Routing System: Geology, v. 45, no. 2, p. 187–190.

SHAOQUAN, X. and SUQING, L., 1996, Review of the Extractive Metallurgy of Scandium in China (1978–1991): Hydrometallurgy, v. 42, p. 337–343.

STEARNS, R.G., 1957, Cretaceous, Paleocene, and Lower Eocene History of the Northern Mississippi Embayment: Geological Society of America Bulletin, v. 68, p. 1077–1100.

TARDY, Y., KOBILSEK, B., and PAQUET, H., 1991, Mineralogical Composition and Geographical Distribution of African and Brazilian Periatlantic Laterites. The influence of Continental-Drift and Tropical Paleoclimates During the Past 150 Million Years and Implications for India and Australia: Journal of African Earth Sciences, v. 12, p. 283–295.

TAYLOR, G., TRUSWELL, E.M., MCQUEEN, K.G., and BROWN, M.C., 1990, Early Tertiary Paleogeography, Landform Evolution, and Paleoclimates of the Southern Monaro, NSW, Australia: Palaeogeography Palaeoclimatology Palaeoecology, v. 78, p. 109–134.

THOMPSON, C.N., 1981, Petrology of North Mississippi Bauxites: A Case For Depositional Bauxite and Kaolin. Unpublished M.S. thesis, University of Mississippi, Oxford, 154 p.

THOMPSON, D.E., 1995, Stratigraphic Framework and Lignite Occurrence in the Paleocene of the Ackerman Area: Mississippi Geology, v. 16, p. 49–59.

TORRÓ, L., PROENZA, J.A., AIGLSPERGER, T., BOVER-ARNAL, T., VILLANOVA-DE-BENAVENT, C., RODRÍGUEZ-GARCÍA, D., RAMÍREZ, A., RODRÍGUEZ, J., MOSQUEA, L.A., and SALAS, R., 2017, Geological, Geochemical and Mineralogical Characteristics of REE-Bearing Las Mercedes Bauxite Deposit, Dominican Republic: Ore Geology Reviews, v. 89, p. 114–131.

TSEKHOVSKY, Y.G., 1987, Sedimentation and Lithogenesis of Humid Redbeds at the Cretaceous/Paleogene Boundary in Kazakhstan, Moscow.

TSEKHOVSKY, Y.G., BOGATYREV, B.A., ZHUKOV, V.V., and YAPASKURT, O.V., 2008, The Role of Endogenous and Exogenous Processes in the Formation of Bauxites: Izvestiya Akademi Nauka, Seriya Khimicheskaya, v. 16, p. 65–82.

UJACZKI, É., COURTNEY, R., and CUSACK, P., 2019, Recovery of Gallium from Bauxite Residue Using Combined Oxalic Acid Leaching with Adsorption onto Zeolite: Journal. of Sustainable, Metallurgy, v. 5, p. 262–274.

UNITED STATES DEPARTMENT OF ENERGY, 2010, Criticality Assessments by Element, *in* Chu, S. (eds.), Critical Materials Strategy: ISBN 978-1-4379-4418-1

VALETON, I., 1972, Bauxites, Elsevier Publishing Company, Amsterdam, 226 p.

VALETON, I., 1999, Saprolite-Bauxite Facies of Ferralitic Duricrusts on Palaeosurfaces of Former Pangaea, *in* Thiry, M., and Simon-Coincon, R. (eds.), Palaeoweathering, Palaeosurfaces, and Related Continental Deposits: Alden Press, p. 153–188.

VAN GOSEN, B.S., and CHOATE, L.M., 2019, Geochemical Analyses of Bauxite and Associated Rocks from the Arkansas Bauxite Region, Central Arkansas: United States Geological Survey Data Release.

ZARASVANDI, A., CARRANZA, E.J.M., ELLAHI, S.S., 2012, Geological, geochemical, and mineralogical characteristics of the Mandan and Deh-now bauxite deposits, Zagros Fold Belt, Iran Ore Geology Review, v. 48, p. 125–138.

ZHANG, R., GONG, E. WANG, G., and YANG, Z., 2018, An Analytical Shortcut to Estimate Alumina Content by LOI in Lateritic Gibbsite Bauxite Prospecting: Aluminum Quality Workshop Inc. 5 p.

APPENDIX

Appendix 1: Additional Field Photos

Figure 1.1. Photographs of the Arrow Road location in May 2018 (top) and December 2020 (bottom).

Figure 1.2. A photograph showing the contact between the interpreted friable fragmental unit and the lateritic duricrust.

Figure 1.3. A photograph showing the second outcrop at Arrow Road.

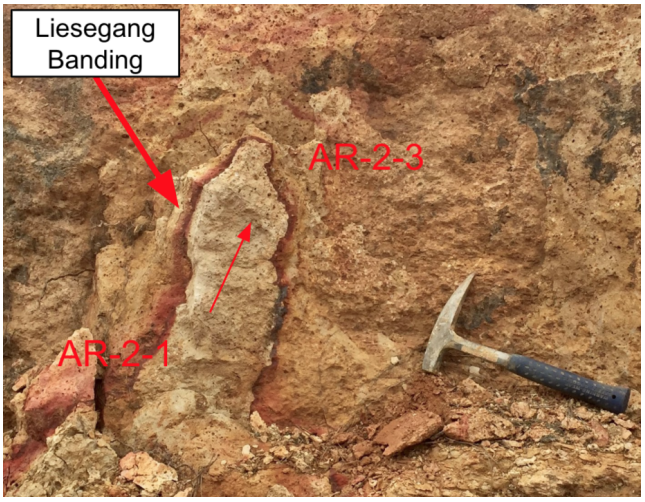

Figure 1.4. Photographs of a second outcrop at the Arrow Road location. Although only partially-exposed, this outcrop displays Liesegang banding at a greater wavelength than the main outcrop at Arrow Road.

Figure 1.5. A photograph showing Third Hill. Bauxite is intermittently exposed by gullies.

Appendix 2: X-Ray Diffractograms

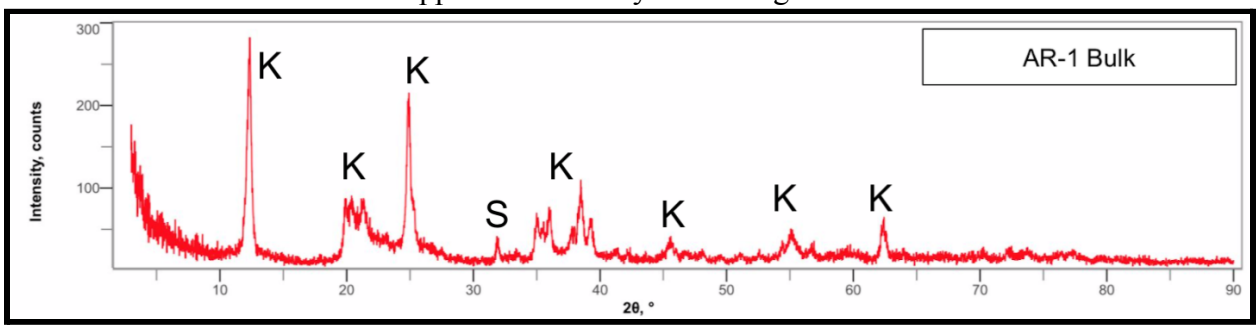

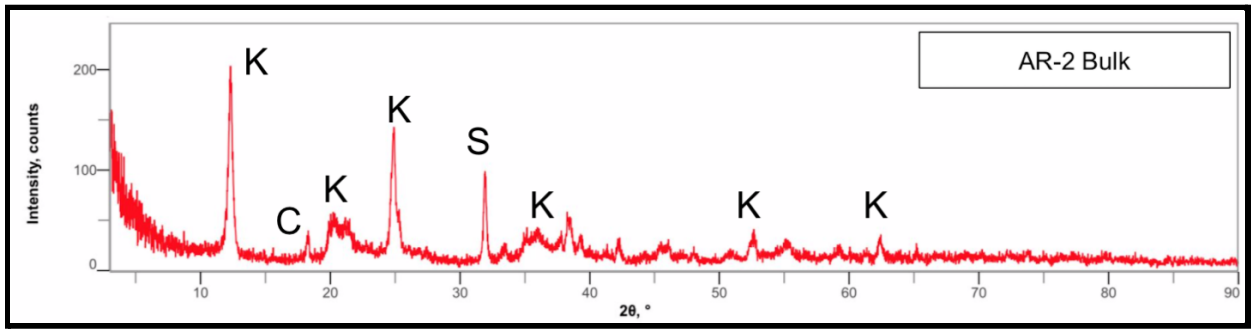

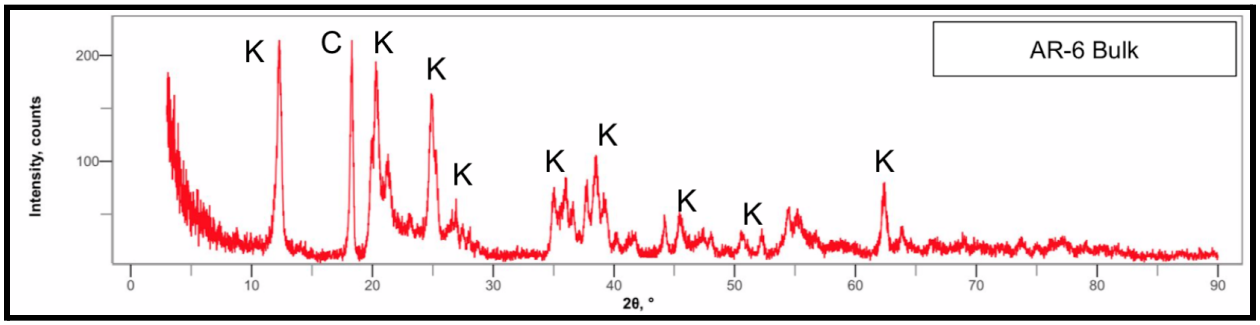

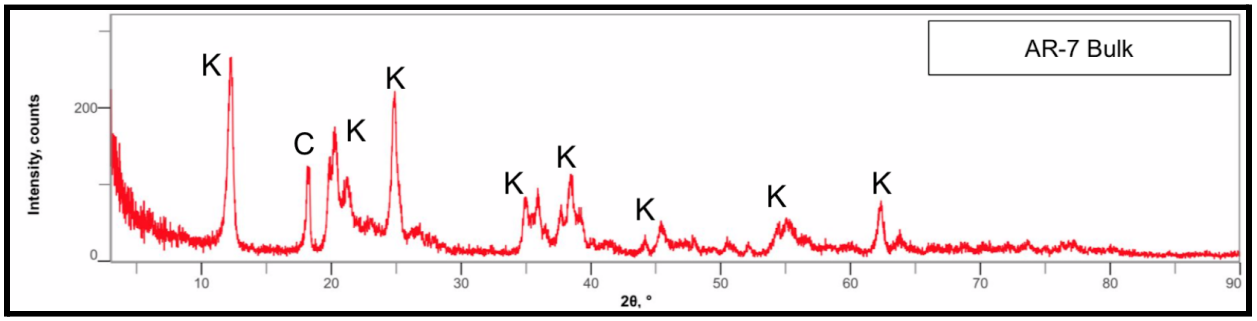

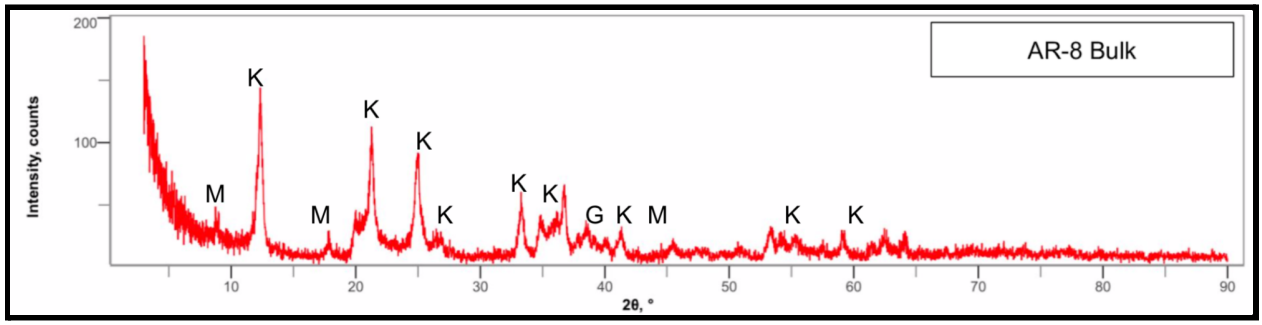

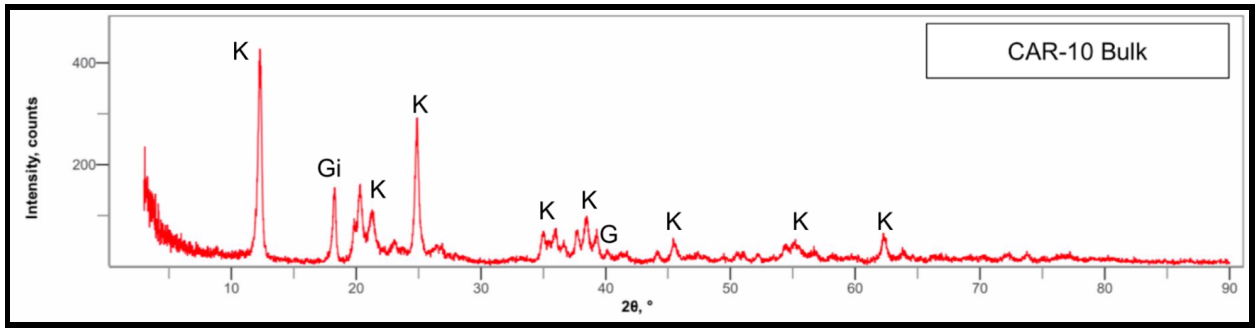
CAR-10 Bulk
Intensity, counts
2θ, °
K
Gi
K
K
K
K
G
K
K
K

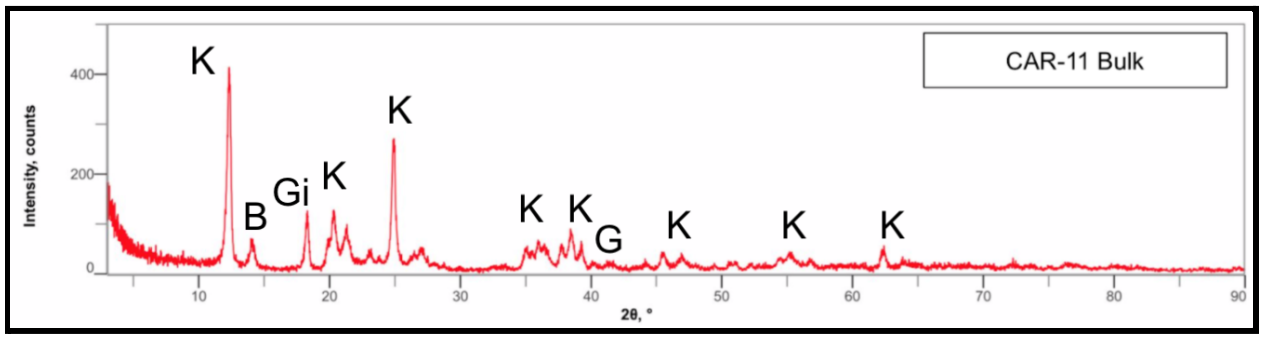
CAR-11 Bulk
Intensity, counts
2θ, °
K
B
Gi
K
K
K
K
G
K
K
K

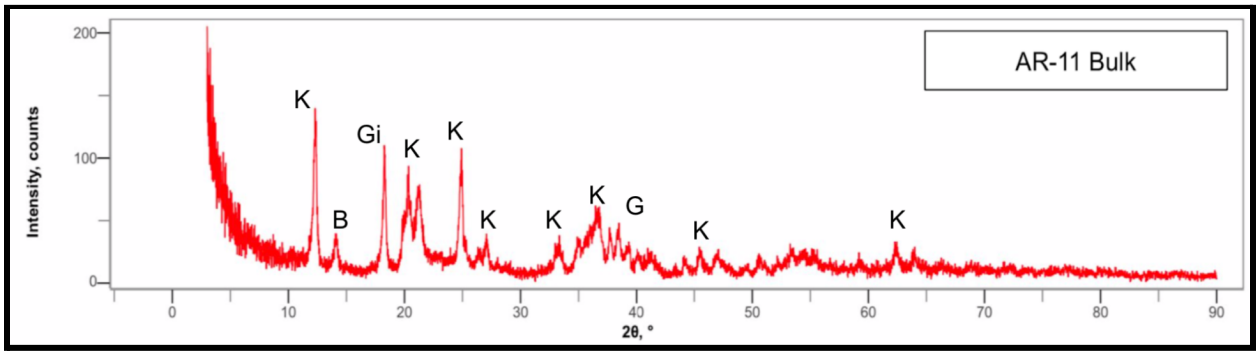
AR-11 Bulk
Intensity, counts
2θ, °
K
B
Gi
K
K
K
K
G
K
K

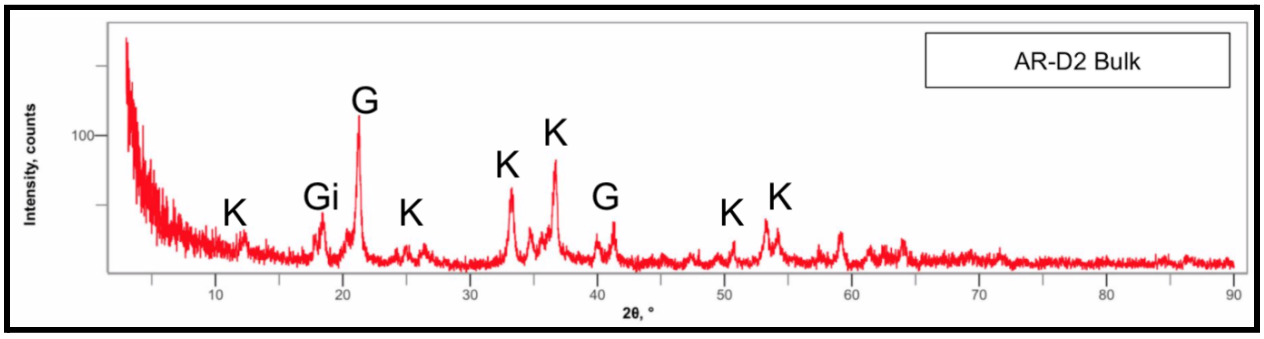
AR-D2 Bulk
Intensity, counts
2θ, °
K
Gi
G
K
K
K
G
K
K

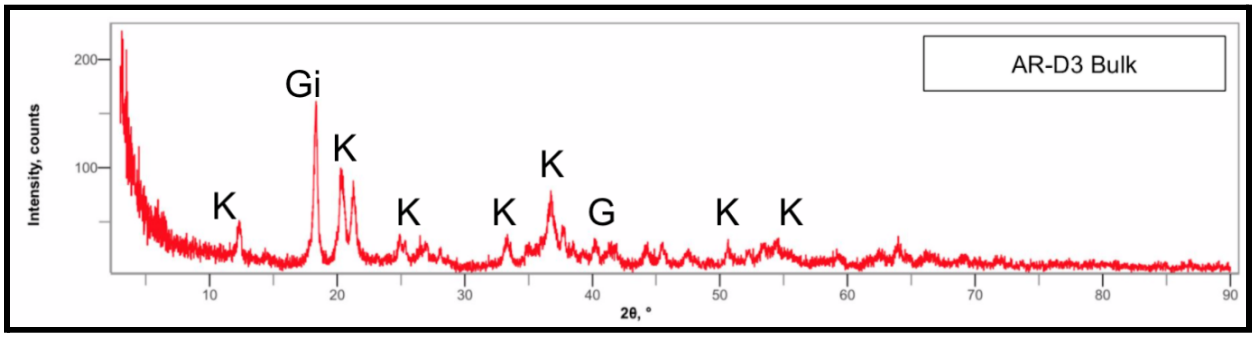
AR-D3 Bulk
Intensity, counts
2θ, °
K
Gi
K
K
K
K
G
K
K

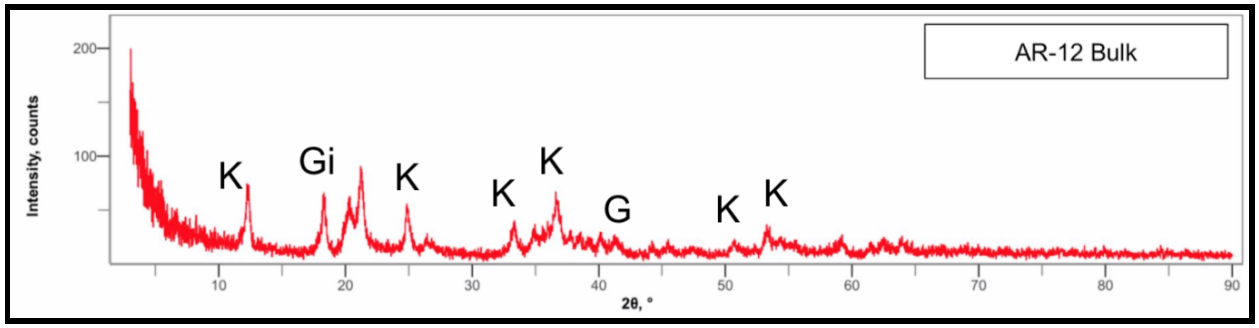
AR-12 Bulk
Intensity, counts
2θ, °
K
Gi
K
K
K
G
K
K

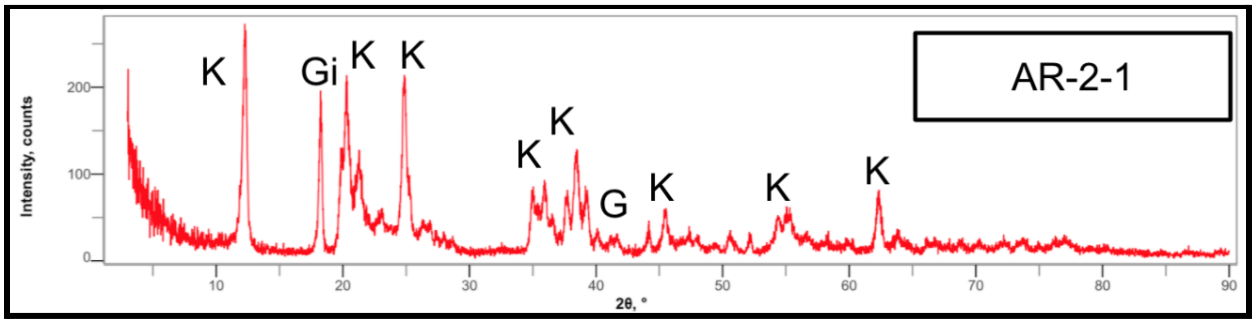
AR-2-1
Intensity, counts
2θ, °
K
Gi
K
K
K
K
G
K
K
K

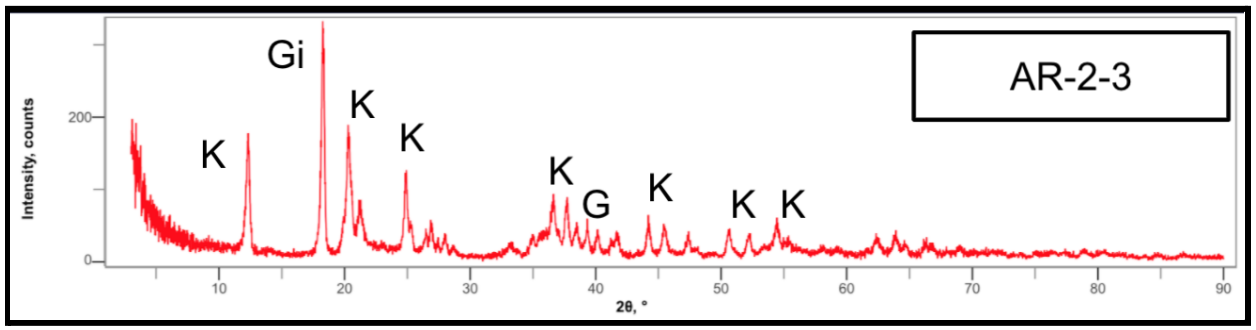
AR-2-3
Intensity, counts
2θ, °
Gi
K
K
K
K
G
K
K
K

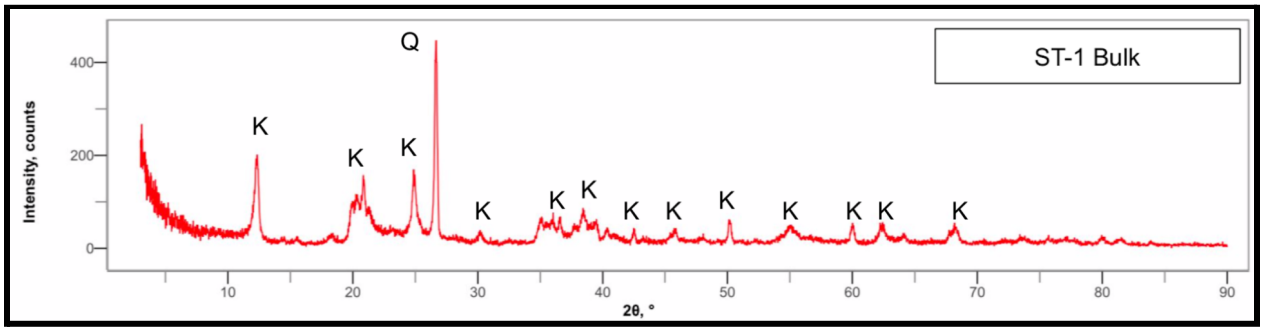
ST-1 Bulk
Intensity, counts
2θ, °
Q
K
K
K
K
K
K
K
K
K
K
K
K
K

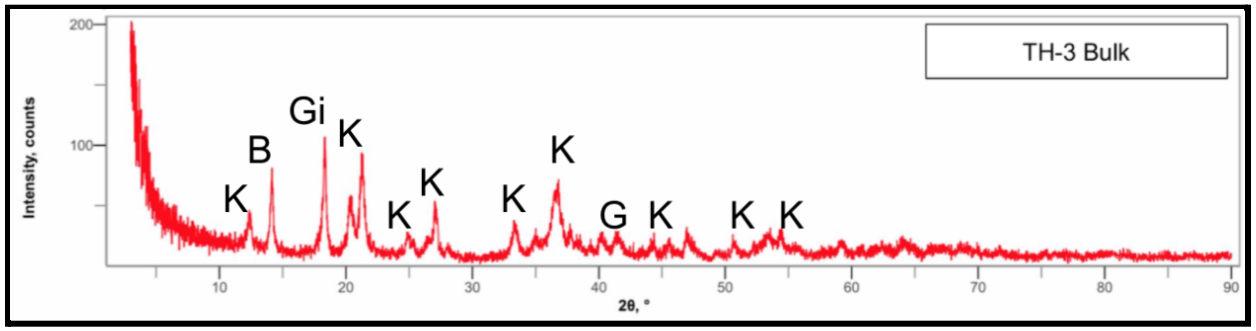
TH-3 Bulk
Intensity, counts
2θ, °
Gi
B
K
K
K
K
K
K
G
K
K
K

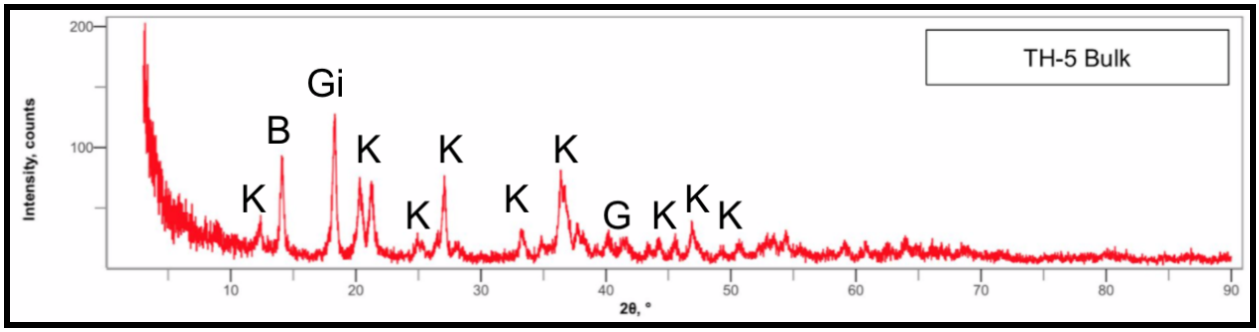
TH-5 Bulk
Intensity, counts
200
100
2θ, °
10
20
30
40
50
60
70
80
90
K
B
Gi
K
K
K
K
K
G
K
K
K

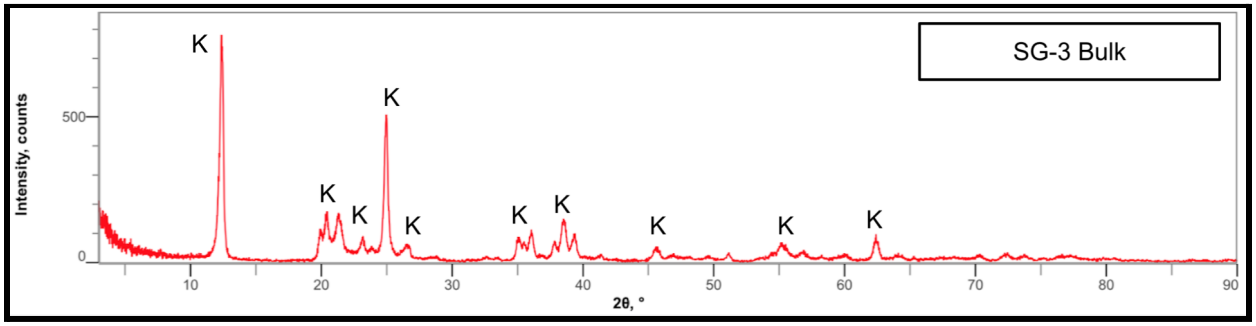
SG-3 Bulk
Intensity, counts
500
0
2θ, °
10
20
30
40
50
60
70
80
90
K
K
K
K
K
K
K
K
K
K

Appendix 3: Additional SEM-EDS Images

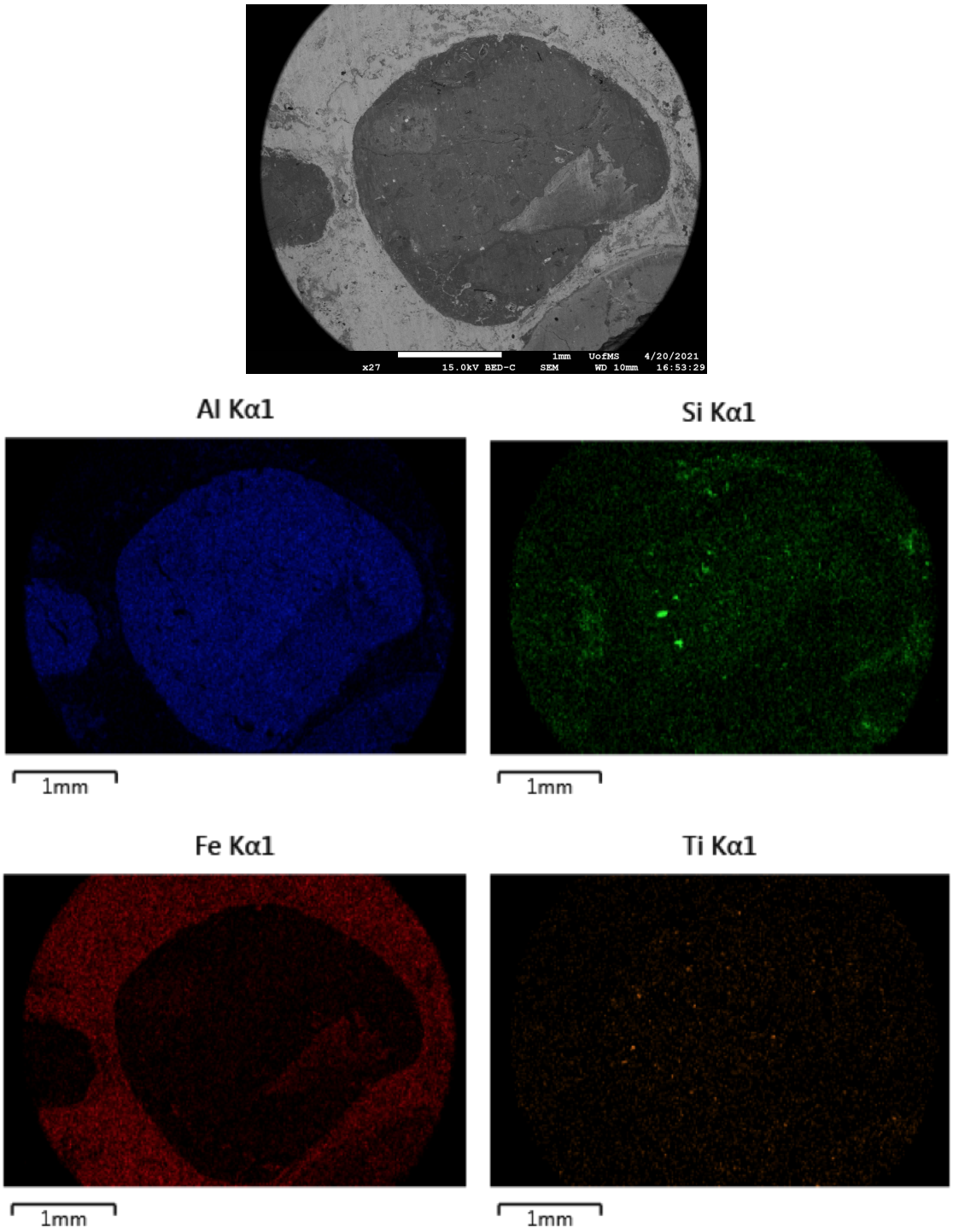

Figure 3.1. SEM-EDS image of sample TH-5 showing three Al-rich pisoliths in an iron-rich matrix.

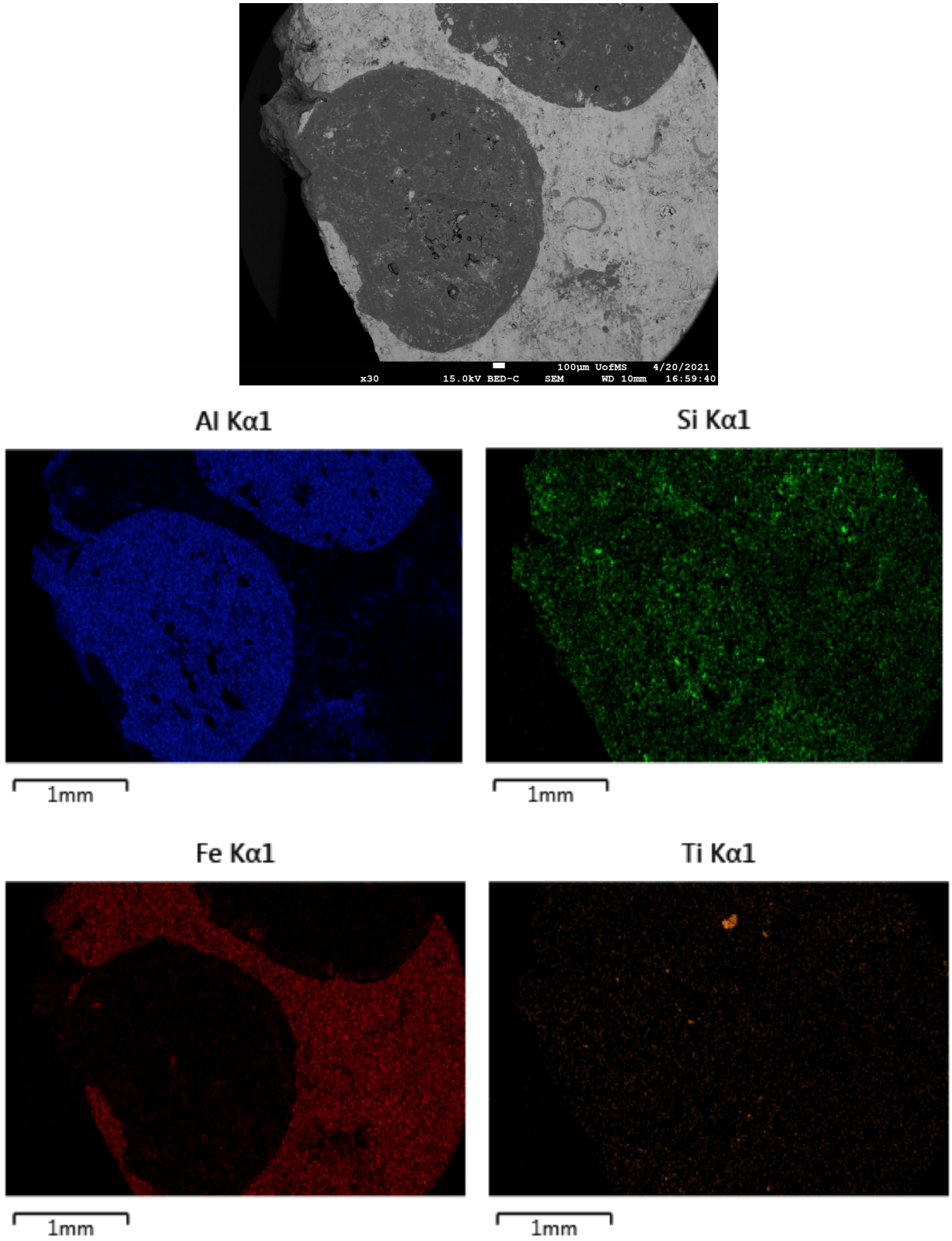

Figure 3.2. SEM-EDS image of sample TH-5 showing two Al-rich pisoliths in an iron-rich matrix.

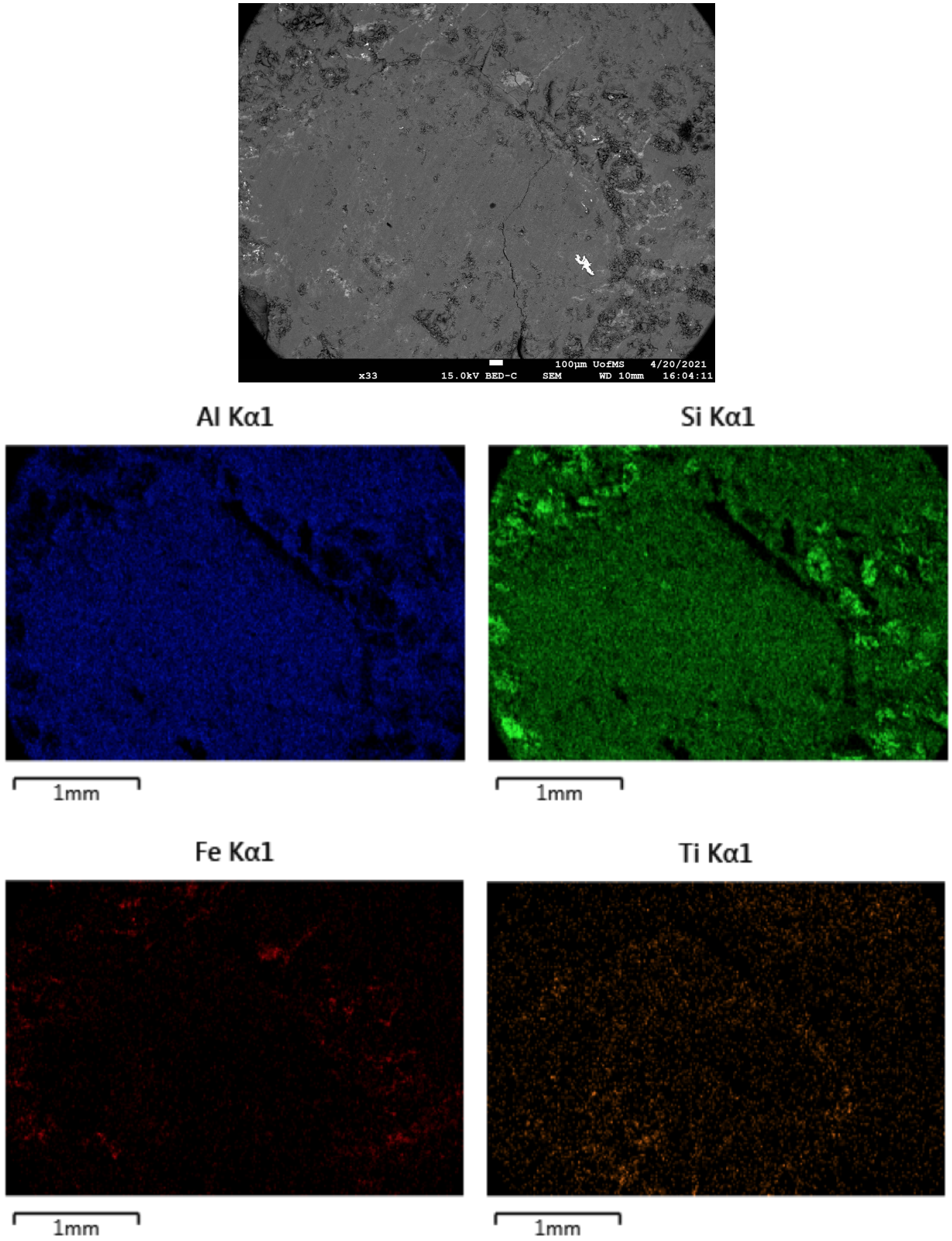

Fig. 3.3. SEM-EDS image of sample ST-1 showing an Al- and Si-rich pisolith in a Si-rich matrix.

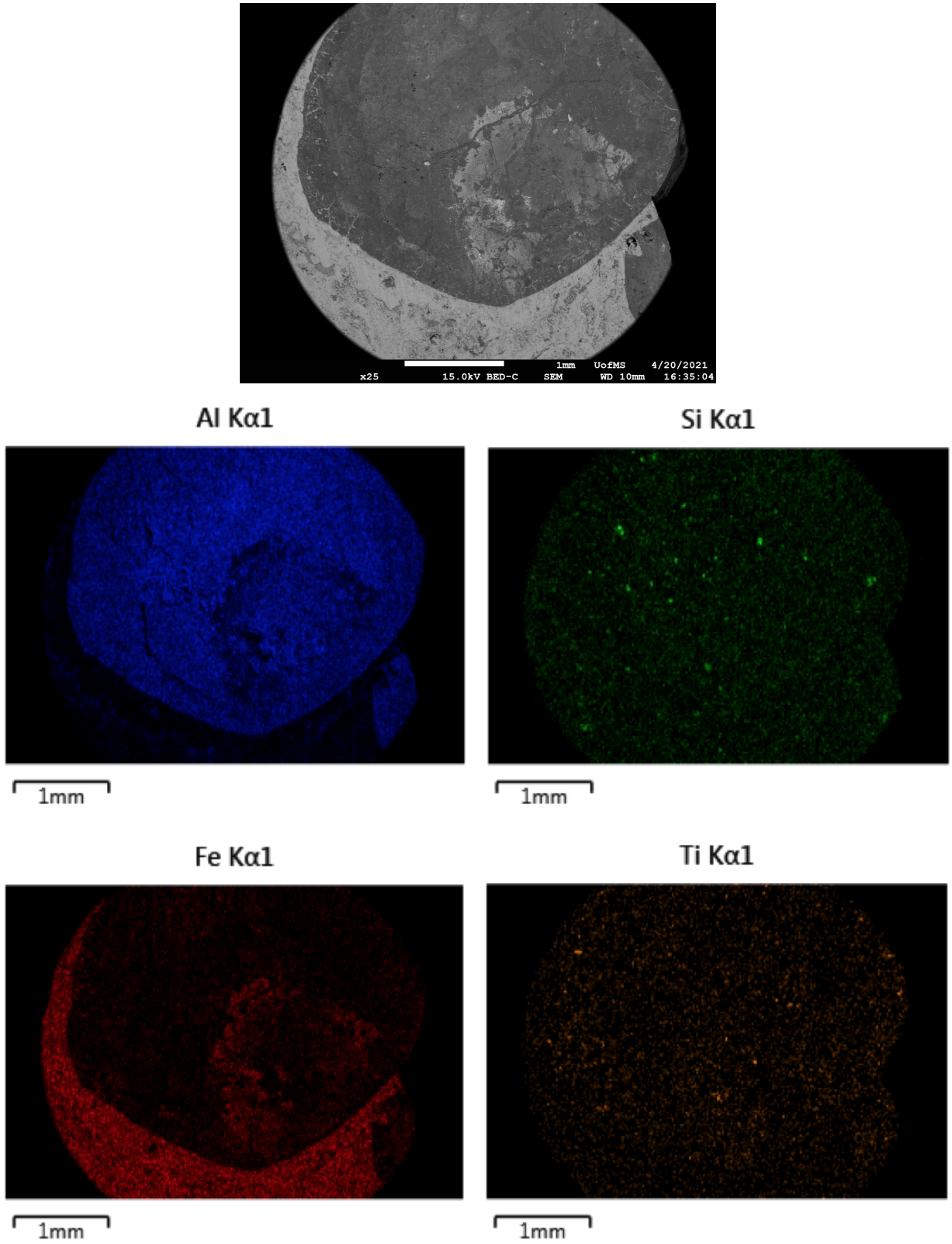

Fig. 3.4. SEM-EDS image of sample TH-5 showing one Al-rich pisoliths in an iron-rich matrix.

VITA

Timothy B. Clark

EDUCATION

Master of Science in Engineering Science - emphasis in Geology, at the University of Mississippi, August 2019 – August 2021. Thesis title: "Stratigraphy and Geochemistry of Paleocene-aged Bauxite from North Mississippi."

Bachelor of Arts in Geological Sciences - minor in Mathematics, at the State University of New York College at Geneseo, August 2015 – May 2019

EMPLOYMENT

Geologist, Sterling Environmental Engineering, P.C., June 2021 - Present. Responsibilities include: Conducting Phase I and II Environmental Site Assessments as well as completing groundwater monitoring and sampling.

Student Contract Worker, Mississippi Department of Environmental Quality, October 2020 - May 2019. Responsibilities included: Completing wastewater sampling and ensuring compliance with state regulations.

Graduate Teaching Assistant, Department of Geology and Geological Engineering, the University of Mississippi, August 2019 - May 2021. Responsibilities include: Assisting with the preparation of undergraduate laboratory courses, grading, and conducting lab activities.

Undergraduate Teaching Assistant, Department of Geological Science, the State University of New York College at Geneseo, August 2017 - December 2018. Responsibilities include: Assisting with the preparation of undergraduate laboratory courses, grading, and conducting lab activities.